Understanding the mechanisms of intergranular corrosion in 2024 Al alloy at the polycrystal scale

Emilie Mondou, Arnaud Proietti, Cédric Charvillat, Cyril Berziou, Xavier Feaugas, David Sinopoli, Christine Blanc

To cite this version:

Emilie Mondou, Arnaud Proietti, Cédric Charvillat, Cyril Berziou, Xavier Feaugas, et al.. Understanding the mechanisms of intergranular corrosion in 2024 Al alloy at the polycrystal scale. Corrosion Science, 2023, 221, pp.111338. 10.1016/j.corsci.2023.111338 . hal-04286491

HAL Id: hal-04286491
https://hal.science/hal-04286491v1

Submitted on 9 Jul 2025

Version of Record: https://www.sciencedirect.com/science/article/pii/S0010938X23003803
Manuscript_4f6fd5eeb7c199d884c6a3f4eabc040d

Understanding the mechanisms of intergranular corrosion in 2024 Al alloy at the polycrystal scale

Emilie Mondou[a], Arnaud Proietti[b], Cédric Charvillat[a], Cyril Berziou[c], Xavier Feaugas[c], David Sinopoli[d], Christine Blanc[a,*]

[a]CIRIMAT, Université de Toulouse, CNRS, INP – ENSIACET, 4 allée Emile Monso – CS 44362, 31030 Toulouse cedex 4, France

[b]Centre de Microcaractérisation R. Castaing, UAR 3623, Espace C. Ader, 3 rue Caroline Aigle, 31400 Toulouse, France

[c]LaSIE, La Rochelle Université, 23 avenue Albert Einstein, BP 33060, 17031 La Rochelle, France

[d]Airbus Helicopters S.A.S., N1 le Bayard, Aéroport international Marseille Provence, 13 725 Marignane Cedex, France

*Corresponding author. Tel./fax: +33 (0)5 34 32 34 07 / +33 (0)5 34 32 34 98

E-mail address: christine.blanc@toulouse-inp.fr

Abstract - This paper provides a new insight into the understanding of the susceptibility to intergranular corrosion (IGC) of 2024 Al alloy. Whatever the exposure conditions, coincidence site lattice high-angle grain boundaries (CSL HAGBs) slightly contributed to IGC damage because of their low contribution to the cumulative length of GBs. Low-angle grain boundaries (LAGBs) showed intrinsic susceptibility to corrosion initiation almost similar to random HAGBs and lower susceptibility to IGC propagation. However, cyclic corrosion tests promoted both corrosion initiation and propagation at LAGBs. This was mostly due to the trapping of corrosion-induced hydrogen in the core of the dislocations defining the LAGBs.

Keywords: A. aluminium alloy; B. EBSD; B. cyclic corrosion tests; C. hydrogen absorption; C. grains boundaries; C. intergranular corrosion.

1. Introduction

Intergranular corrosion (IGC) is a form of corrosion widely encountered in industrial applications, in particular in the aeronautical sector. It constitutes one of the major bottlenecks towards longevity for metallic structural parts, in such a way that the development of highly IGC-resistant metallic materials will constitute a meaningful improvement for various industrial fields. Many studies have shown that the susceptibility to IGC of metallic materials significantly depends on the nature of the grain boundaries (GBs) [1-3], leading to the development of grain boundary engineering as a relevant solution to overcome the issues of durability raised by the IGC damage [4-9]. In general, whatever the materials, the authors agree that low-angle grain boundaries (LAGBs) are more resistant to IGC than high-angle grain boundaries (HAGBs) [1,2,10-14]. However, the IGC susceptibility of random HAGBs (RHAGBs) compared to coincidence site lattice (CSL) HAGBs remains controversial: some authors showed that CSL HAGBs were more resistant to IGC than RHAGBs and proposed that increasing the ratio of CSL HAGBs in a metallic material would improve its resistance to IGC [3,15,16], while others concluded that both types of GBs had the same susceptibility to IGC [1,12].

The origin of the differences in IGC susceptibility between the different types of GBs is still a largely debated issue. A first approach consists in considering that the susceptibility to IGC of the GBs was mostly due to the segregation of alloying elements at the GBs and/or to the presence of precipitates. In aluminium alloys, galvanic coupling between the intergranular precipitates, the precipitate free zone (PFZ) and the surrounding matrix was often considered as a relevant explanation for IGC mechanisms [17-23]. Therefore, numerous studies focused on the electrochemical behaviour of intergranular precipitates, *e.g.* Al-Cu-Mg precipitates that present an anodic behavior compared to the matrix, while Al_2Cu and Al-Cu-Mn-Fe precipitates act as a local cathode [17,24]. However, literature data clearly showed that other metallurgical parameters had to be considered to explain the IGC susceptibility of a GB, *e.g.*, their level of misorientation, their energy and/or the excess volume, and the stored energy in the surrounding grains [11,14,21,25,26], but the intricate interplay between all these parameters is not fully elucidated. Many studies showed that there was a strong relationship between the susceptibility to IGC of the GBs, their level of misorientation and their precipitation state [1,2,27-29]. For example, literature showed that LAGBs had more discontinuous precipitation than HAGBs, explaining their lower susceptibility to IGC [28]. Meanwhile, other authors showed that the precipitation state at the GBs did not play a major role in IGC [11,14,25,26]. For Zhang *et al.*, dissolution occurred at the GBs, mostly because they constituted a defect, and the lower susceptibility to IGC of LAGBs was explained due to the similar orientation of the abutting grains of the GB [14].

Then, considering the exposure conditions of the metallic materials to the environment makes the understanding of the IGC mechanisms even more complex. Indeed, literature data clearly showed that the IGC susceptibility of the GBs was strongly dependent on the exposure conditions [30-33]; for example, an increase in the IGC susceptibility of both HAGBs and LAGBs was observed after cyclic exposures to the environment compared to continuous immersions [30-35]. These differences could be explained by the increase in the electrolyte concentration, *i.e.* in the content of aggressive species, inside the IGC defects during emersion phases [31,36]. Hydrogen uptake, following the corrosion reactions, had also to be considered, literature data showing that hydrogen promoted the corrosion reactions [10,37]. The influence of the exposure conditions on the IGC susceptibility of the GBs could contribute to explain the apparent controversy about the IGC susceptibility of RHAGBs compared to CSL HAGBs. Furthermore, it could be noted that the authors often considered the IGC susceptibility from a global point of view, without distinguishing between the initiation and propagation steps of the damage. Giving specific attention to each step of the IGC mechanisms could also allow, at least partially, to better describe the behaviour of each type of GBs.

In the present paper, the susceptibility to IGC of RHAGBs, CSL HAGBs and LAGBs of a 2024 Al alloy was analysed. This alloy was chosen because it is widely used in industry, particularly the aerospace industry. It is susceptible to IGC and has been the subject of numerous studies [10,18-21,23,24,30-32,37]. It was therefore a relevant choice to go further in the quantification of the susceptibility to IGC of the different types of GBs, with a view to providing some answers that could eventually be useful at least for other relatively similar alloys. The aim was to compare and quantify the susceptibility to IGC of the three types of GBs considering, on the one hand, the initiation and propagation steps of IGC, and taking into account, on the other hand, the exposure conditions. The IGC susceptibility of the GBs after continuous immersion and cyclic tests performed in a 5 mM NaCl solution was analysed combining electron backscatter diffraction (EBSD) observations and scanning electron microscope (SEM) in the backscattered electrons (BSE) mode. In view of the above literature review, the IGC susceptibility of the three types of GBs was certainly linked to complex interactions between different metallurgical parameters, e.g. alloying elements, precipitation state and misorientation. However, elucidating the contribution of each metallurgical parameter on the IGC susceptibility of the GBs was not the focus of this paper. The paper focused on the influence of exposure conditions on the IGC susceptibility of the GBs. According to the above literature review, the chloride concentration of the electrolyte trapped inside the IGC defects, as well as the hydrogen uptake, could vary depending on the exposure conditions. Consequently, some experiments were performed for different chloride concentrations in order to assess the influence of this parameter on the IGC susceptibility of the GBs. Scanning kelvin probe force microscopy (SKPFM) and thermodesorption spectroscopy (TDS) experiments were also implemented to investigate further the influence of corrosion –induced hydrogen on the IGC susceptibility of the GBs.

2. Experimental procedure

2.1. Material

The material studied was a 60-mm thick rolled plate of 2024 Al alloy in T351 metallurgical state (hot rolling, solution heat treatment, water quenching, stress relieve and natural ageing at room temperature). Its chemical composition was 4.56 % Cu, 1.37 % Mg, 0.47 % Mn, 0.12 % Fe, 0.14 % Zn (wt. %). Observations using an optical microscope (OM) and a SEM combined with energy dispersive X-ray analyses (EDX) allowed two types of coarse intermetallic particles (IMPs) to be distinguished, *i.e.* Al_2CuMg and Al-Cu-Mn-Fe IMPs, in agreement with the literature [17,19-21,24]. OM observations after chemical etching showed a microstructure gradient perpendicularly to the rolling plane, with recrystallised grains near the rolling plane (skin) and grains elongated in the rolling direction in the core of the plate. In the present study, all samples were removed from the core of the plate where the average grain size was 420, 200 and 55 μm in the longitudinal (L, rolling), long transverse (LT) and short transverse (ST) directions, respectively.

2.2. Corrosion tests

Most of the corrosion tests were performed in a 5 mM NaCl solution. Chloride ions were considered as representative of the chemical environment of aircraft structures; furthermore, it was necessary to use a moderately aggressive electrolyte to allow proper analysis of corroded GBs. The tests consisted in continuous immersions (referred to as CI) with immersion times ranging from 8 h to 168 h. Cyclic tests alternating immersion periods (duration 8 h) and emersion periods (duration 16 h) were also performed. Considering that an immersion period followed by an emersion period constituted an elementary cycle, cyclic tests consisting in 1, 3 and 7 elementary cycles were carried out; they were referred to as 1CR, 3CR and 7CR, respectively. All tests were performed at room temperature (25 °C) using parallelepiped samples (3 (L) x 5 (LT) x 1 (ST) mm^3). For the cyclic tests, the immersion and emersion periods were carried out at room temperature. After an immersion period (8h), the samples were removed from the electrolyte, hanged up using a nylon thread in an empty beaker for 16h (emersion period), before being re-immersed in the electrolyte for the next immersion period. The samples were not rinsed between each period. Before the tests, the samples were embedded in epoxy resin in such a way that only one LT-ST plane (5 x 1 mm^3) was exposed to the electrolyte. Then, they were grounded with SiC paper to grade 4000, polished with 1µm diamond suspension, and finally with a colloidal silica suspension (OPS) with a vibrating plate for 3 h. They were finally rinsed with distilled water and air-dried, before being subjected to EBSD analysis (see section 2.3), and then exposed to the NaCl electrolyte. After the corrosion tests, the samples were rinsed with distilled water and air-dried.

Additional 24hCI tests were also performed in 10 mM and 100 mM NaCl solutions to study the influence of the chloride content on the susceptibility to corrosion of the GBs.

2.3. Quantification of the susceptibility to corrosion of the GBs

A methodology was developed in order to identify the GBs and quantify their susceptibility to corrosion. It included the following steps (Fig. 1): (1) Identification and marking of the zones of interest (3 x 1 mm^2, LT-ST plane) by indentation with a micro-durometer of the non-corroded sample after the grounding and polishing steps described in section 2.2, (2) Identification of the GBs by using EBSD analysis: several grain orientation maps (inverse pole figure, map 1) and the corresponding band contrast maps (map 2) were plotted and assembled to cover the delimited area, (3) Corrosion tests, (4) Mechanical polishing using 1 µm diamond paste to remove the corrosion products, (5) Locating of the corroded GBs using SEM analysis in backscattered electron (BSE) mode: several SEM/BSE maps (map 3) were plotted and assembled to cover the area of interest, (6) Identification of the corroded GBs by superimposition of maps 2 and 3.

EBSD maps and SEM/BSE maps were obtained using a JEOL JSM 7100F field emission gun scanning electron microscope (FEG-SEM) equipped with an EBSD system (Symmetry S2, Oxford Instruments). EBSD data and SEM/BSE data were post-processed with AztecCrystal software (Oxford Instruments) allowing maps 1, 2 and 3 to be obtained. For EBSD analysis, fields of view of 1.8 mm x 0.8 mm in LT-ST plane were used for an accurate analysis of the GBs. The maps were cleaned using the neighbor method before identification of the GBs. Nevertheless LAGBs and HAGBs were identified as local interfaces having a misorientation higher than 2 ° in order to prevent from orientation noise. Brandon criterion of 15 ° was used as critical value for misorientation angle to differentiate LAGBs and HAGBs [1, 38-41]. A distinction was also made between RHAGBs and special HAGBs, *i.e.* CSL HAGBs. ∑n GBs were studied for n values from 3 to 49 (low and high ∑) without distinction between each ∑ [42-43].

The susceptibility to corrosion propagation of the GBs was quantified by measuring the cumulative (total) length of corroded grain boundaries for each type of GBs, and then calculating an index of susceptibility to corrosion propagation referred to as I_{cs}. For a given exposure condition, and for each type of GBs, *i.e.* LAGBs, RHAGBs, and CSL HAGBs, I_{cs}

value was defined as the ratio between the cumulative length of the corroded GBs (of this type) measured on the corroded sample (Fig. 1 map 3 with GBs identified using Fig. 1 map 4) and the cumulative length of the GBs (of this type) measured on the non-corroded sample (Fig. 1 map 2). Moreover, for a given exposure condition, the susceptibility to corrosion initiation of one type of GBs was evaluated by counting the number of corroded GBs of this type. This was done manually by identifying the GBs where an IGC defect had formed; this was highly time-consuming but possible. However, it should be mentioned here that it was not possible to determine the number of each type of GBs for the non-corroded sample, because the GBs form a complex network where it is not possible to distinguish where a GB of a given type begins and ends. In other words, the end of a given type of GB is defined by the transition to another type of GB. It was therefore not possible to calculate an index of susceptibility to corrosion initiation. To this end, the susceptibility to corrosion initiation was evaluated by analysing the evolution of the number of corroded GBs as immersion time increased, or as the chloride concentration increased.

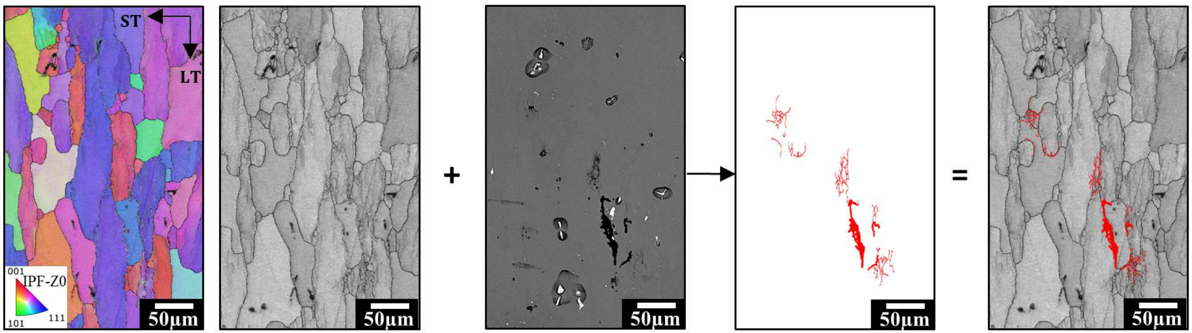

Map 1
Identification of grain orientation
EBSD

Map 2
Identification of the nature of the GBs
EBSD

Map 3
Localisation of corrosion defects
SEM/BSE

Map 4
Corroded surface Superimposition of maps 2 and 3

Fig. 1. *Identification of the nature of the corroded GBs using EBSD analysis (inverse pole figure and band contrast figure with LAGBs, RHAGBs and CSL HAGBs) of a non-corroded sample combined with SEM/BSE image of the same area after corrosion test.*

Map 3 in Fig. 1 shows that some of the corroded GBs were interconnected (i.e. some corroded GBs were connected to other corroded GBs) and formed a complex network of corroded GBs, which could include corroded RHAGBs, LAGBs and CSL HAGBs. As previously mentioned, each corroded GB was counted to assess the susceptibility to corrosion initiation of each type of GBs. However, in order to complete the description of the IGC damage, in particular to highlight the branching of IGC defects, the networks of corroded GBs, referred to as corroded areas, were also counted (Fig. 2).

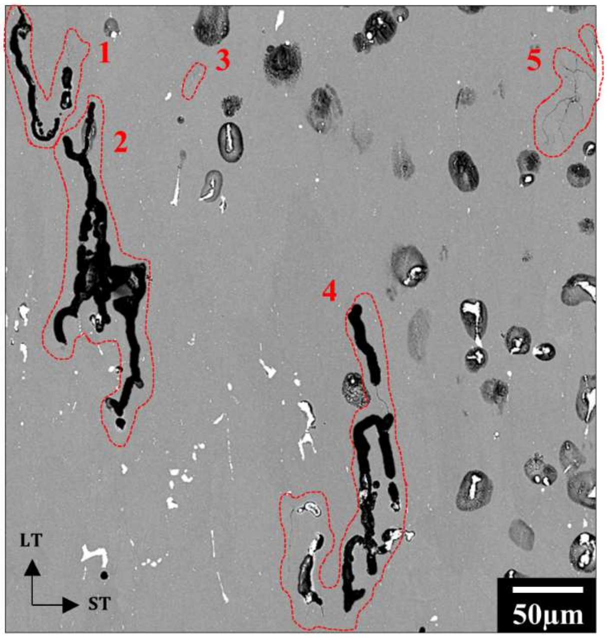

Fig. 2. *SEM observation of a corroded sample and identification of the corroded areas (5 corroded areas are counted here).*

2.4. Evaluation of the contribution of hydrogen to the corrosion kinetics

The hydrogen uptake following the corrosion tests was evaluated by measuring the global hydrogen amount of corroded samples using a melting method with a Bruker G8 GALILEO Instrumental Gas Analyzer. Small coupons of 8 (L) x 10 (LT) x 1 (ST) mm^3 were used for these measurements. They were grounded and polished as described in section 2.2. before the corrosion tests. They were also slightly polished after the corrosion tests and before measurements of the hydrogen content in order to remove the corrosion products.

TDS analyses of corroded samples were also performed to contribute to the understanding of the influence of hydrogen on the IGC susceptibility of the GBs. Experiments were performed using a Jobin Yvon Horiba EMGA-621 W hydrogen analyser: it was composed of an impulsion furnace system combined with a thermal conductivity detector. The temperature range was [30–1100] °C, and the heating rate was 110 °C min^{-1}. The corroded samples were 5 (L) x (16) LT x 1 (ST) mm^3 parallelepipeds that had been subjected to 24hCI, 72hCI and 3CR corrosion tests. Before TDS analyses, they were slightly polished to remove the corrosion products as for the hydrogen content measurements. Furthermore, before each TDS experiment, a preliminary analysis was performed with an empty crucible, and the signal obtained in this condition was substracted from the signal recorded with the corroded samples.

Finally, SKPFM maps were also plotted to analyse the distribution of hydrogen inside the corroded sample. The interest of SKPFM to detect and locate hydrogen inside a material has been demonstrated in previous studies [44-46]. In the present study, SKPFM measurements were performed, in air and at room temperature, using a BRUKER Icon AFM instrument equipped with a NanoScope V controller, and NanoScope version 9.7 software (Bruker, Santa Barbara, California). Topography maps were acquired in a first pass in a PeakForce Tapping mode and the SKPFM signal was acquired in a second pass with a lift of 100 nm between the probe and the sample surface. The cantilever used is a PFQNE-Al conductive silicon tip (BRUKER) with a nominal radius of 5 nm and a nominal spring constant of 0.8 N/m. In the PeakForce Tapping mode set up, the tip was oscillating at 2 kHz (off resonance), the peak force tapping amplitude was set to 150 nm and the peak force threshold was varied throughout the scan (ScanAsyst mode). In the second pass, SKPFM with amplitude modulation was used, as described in our previous work [45]. Data treatments and profiles extractions were performed with the Nanoscope Analysis software (Bruker). The corroded samples were 8 (L) x (10) LT x 1 (ST) mm^3 parallelepipeds that had been subjected to 24hCI and 1CR corrosion tests. Before SKPFM maps, they were slightly polished to remove the corrosion products as for the hydrogen content measurements and TDS analyses. Areas of interest were marked by indentation using a micro-durometer; SKPFM maps were plotted on corroded samples immediately after slight polishing, but also after heat treatments allowing hydrogen desorption.

3. Results and discussion

3.1. Analysis of the grain boundary character distribution (GBCD) of the 2024 Al alloy

Fig. 3 shows a band contrast map plotted for the non-corroded 2024 Al alloy (LT-ST plane) where LAGBs, RHAGBs and CSL HAGBs are colored in grey, black and red color, respectively. This figure is characteristic of a deformed sample with grains elongated in the rolling direction; the large amount of LAGBs suggested a high level of internal misorientation, *i.e.* high stored energy, due to the rolling process, and could be associated with recovery process occurring during the rolling step [47,48]. Furthermore, the presence of small equiaxed grains (bottom part of Fig. 3), free of LAGBs, could be interpreted as the onset of a recrystallisation process [47].

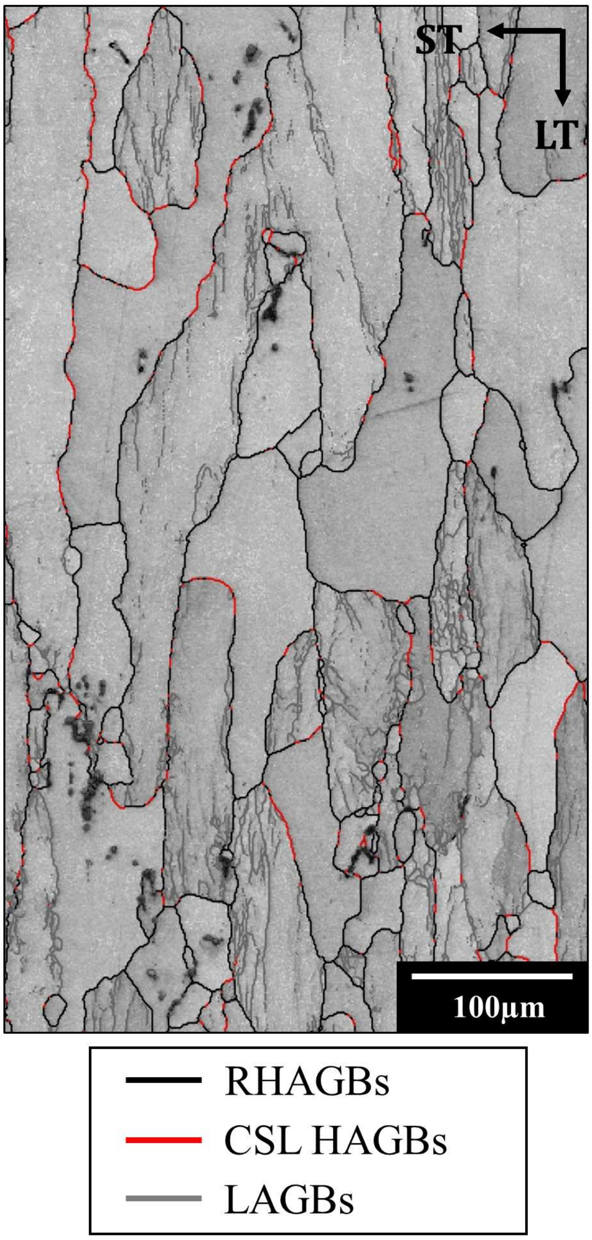

Fig. 3. *Band contrast map obtained by EBSD for the non-corroded 2024 Al alloy sample, where LAGBs (grey lines), RHAGBs (black lines) and CSL HAGBs (red lines) can be distinguished.*

Fig. 4 gives a quantitative description of the GBCD of the 2024 Al alloy: the frequencies in Fig. 4a, and the fraction of each type of GBs in Fig. 4b were calculated by considering the cumulative length of the GBs as a function of their level of misorientation (Fig. 4a) and for each type of GBs (Fig. 4b). Fig. 4b shows a large proportion of LAGBs, which constituted nearly 50 % of the GBs, as suggested by Fig. 3. The result was in agreement with literature data obtained for the same alloy [10]. Furthermore, for a better description of the GBCD, the respective amounts of RHAGBs and special HAGBs, *i.e.* CSL HAGBs, were also calculated. The CSL HAGBs represented only one fifth (in length) of the HAGBs, which was also in agreement with the literature [10]. Most parts of the CSL HAGBs were Σ3 GBs; however, in the following, no distinction was made between the different types of CSL HAGBs concerning their susceptibility to corrosion.

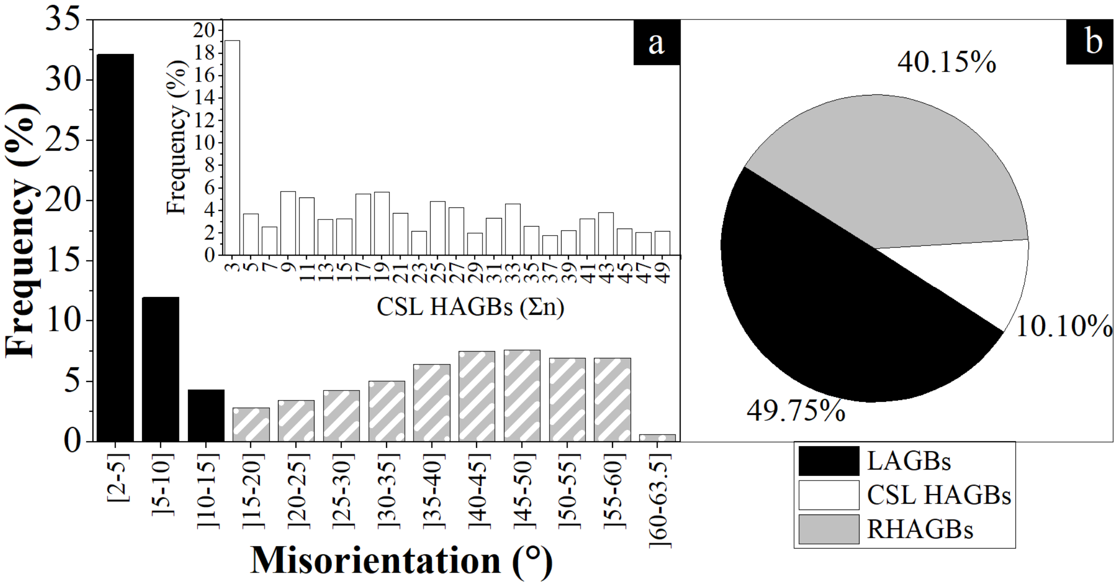

Fig. 4. *a) Distribution (in cumulative length) of the GBs present in the non-corroded 2024 Al alloy as a function of their level of misorientation. The insert shows the distribution (in cumulative length) of the CSL HAGBs. b) Total fractions of LAGBs, RHAGBs and CSL HAGBs calculated by considering the cumulative length of each type of GBs.*

3.2. Qualitative evaluation of the corrosion susceptibility of the GBs in 2024 Al alloy

Fig. 5 shows SEM observations of the samples (LT-ST planes) after CI tests with duration times of 8 h, 24 h, 72 h and 168 h, and after 1CR, 3CR and 7CR tests. For CI and CR tests, dissolution of the matrix around the IMPs and IGC defects were observed, showing that the

2024 Al alloy was susceptible to pitting corrosion associated with IMPs and intergranular corrosion, in agreement with the literature [24,18]. For CI tests (Fig. 5a to d), the IGC defects were found to be longer, and more and more branched when the immersion time in the NaCl solution increased. Considering the previous analysis of the GBCD of the sample and comparing Fig. 5 with Fig. 3 (where the different types of GBs are identified), it seemed that, for short immersion times, the corroded GBs were mainly RHAGBs (Fig. 5a), whereas, for longer immersion times, numerous LAGBs were also corroded (Fig. 5c and d). Therefore, the results suggested that the corrosion first occurred at HAGBs, and then extended to LAGBs, leading to a modification of the morphology of the IGC defects. This did not exclude that some LAGBs could be corroded even for short immersion times, and could be explained either by considering that LAGBs were less susceptible to corrosion initiation than RHAGBs, or that they were less susceptible to corrosion propagation in such a way as, for short immersion times, most part of the corrosion damage seemed to be localised at the RHAGBs. Overall, without distinguishing at this stage between the initiation step and the propagation step of the IGC mechanisms, the result suggested that LAGBs were intrinsically less susceptible to corrosion than HAGBs, in agreement with the literature [1,2,10-12,49], and that their corrosion susceptibility increased with the immersion time in the NaCl solution.

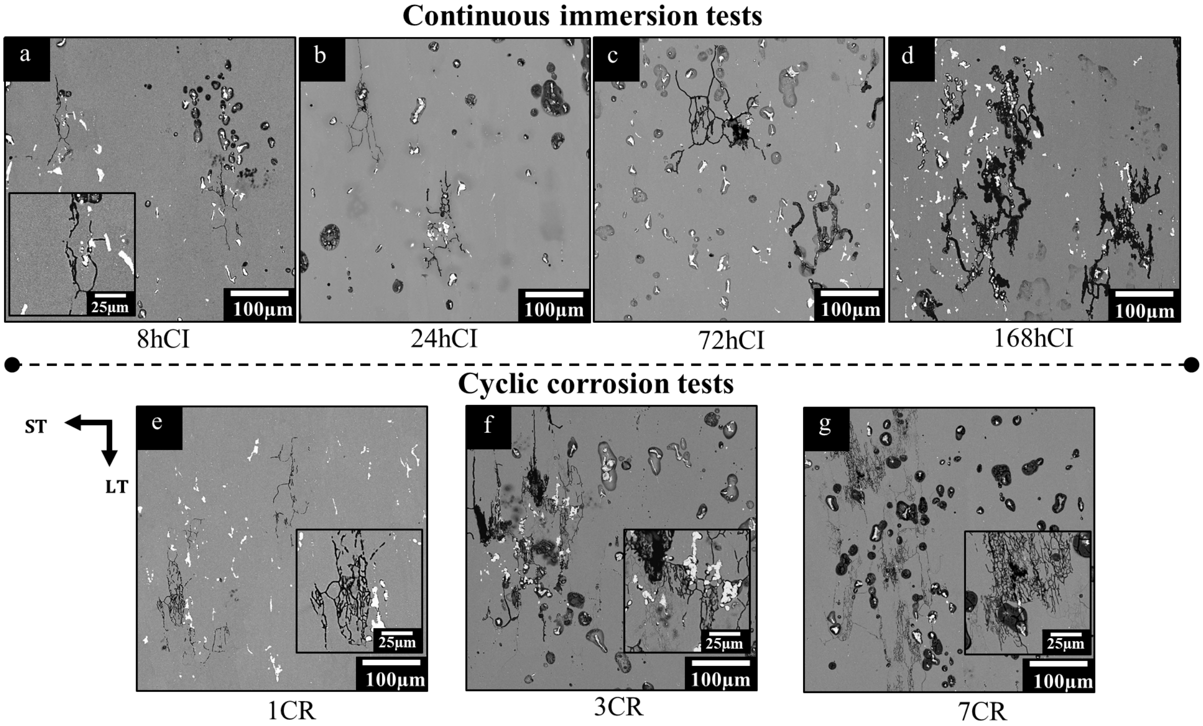

Fig. 5. *BSE-SEM images of the 2024 Al alloy after continuous immersion tests in 5 mM NaCl with various immersion times a) 8 h, b) 24 h, c) 72 h and d) 168 h, and after cyclic corrosion tests with e) 1 elementary cycle, f) 3 elementary cycles and g) 7 elementary cycles. Elementary cycle = 8 h immersion in 5 mM NaCl + 16 h emersion in air.*

Attention was then given to the samples exposed to CR tests. It was of interest to note that the total duration of immersion was 8 h, 24 h and 56 h for 1CR, 3CR and 7CR tests, respectively, while the total duration of these tests was 24 h, 72 h and 168 h for 1CR, 3CR and 7CR tests, respectively. Comparison of the SEM images obtained for 1CR sample (Fig. 5e) and 8hCI sample (Fig. 5a) clearly showed that, for the same duration of immersion, the IGC defects formed after a CR test were more branched than those formed after a CI test. The same conclusion was done by comparing 3CR (Fig. 5f) with 24hCI (Fig. 5b) SEM images, and 7CR (Fig. 5g) with 72hCI (Fig. 5c) SEM images, the latter comparison showing that, even for a shorter immersion time, CR tests led to significantly more branched IGC defects than CI tests. This showed that CR tests were more aggressive than CI tests, in agreement with the literature [18,31]. Furthermore, the results showed that the corrosion susceptibility of the GBs depended on the exposure conditions, with CR tests significantly promoting the corrosion of LAGBs and leading to a branching of the IGC defects, even for short immersion times.

3.3. Quantitative evaluation of the corrosion susceptibility of the GBs in 2024 Al alloy

To validate the qualitative analysis of the corrosion susceptibility of the GBs, and for a more accurate understanding of the IGC susceptibility of 2024 Al alloy, the susceptibility to corrosion of the different types of GBs was quantified using the methodology described in the experimental section (Fig. 1). Attention was given to the initiation and propagation steps of the corrosion phenomenon.

As indicated in section 2.3, the susceptibility to corrosion initiation of a type of GB was quantified by counting the number of corroded GBs of the given type. Fig. 6a, b and c shows the results obtained for LAGBs, CSL HAGBs and RHAGBs, respectively, for continuous immersion tests and cyclic corrosion tests. First, results showed that, for all GBs, the number of corroded GBs increased with the immersion time for continuous immersion tests, showing that the initiation of new IGC defects contributed to the extent of the corrosion damage during a period of time simultaneously with the propagation of existing IGC defects. Then, results clearly showed that, regardless of the exposure conditions, the number of corroded CSL HAGBs was lower than that of LAGBs and RHAGBs. This suggested a low contribution of CSL HAGBs to the corrosion damage for both continuous immersion tests and cyclic corrosion tests. This could be explained either by a lower susceptibility to corrosion initiation of CSL HAGBs compared to LAGBs and RHAGBs, or simply by the fact that CSL HAGBs represented only 10,10 % of the total length of GBs in the non-corroded sample (Fig. 4) in such a way as the probability to initiate corrosion at CSL HAGBs was statistically lower. By studying the evolution of the number of corroded GBs as the immersion time increased, it was possible to assess the susceptibility to corrosion initiation of each type of GBs. For continuous immersion tests, the number of corroded GBs was multiplied by 1.6, 2.4 and 2.4 for LAGBs, CSL HAGBs and RHAGBs, respectively, between 8hCI and 72hCI. This suggested similar susceptibility to corrosion initiation for CSL HAGBs and RHAGBs, and a slightly lower susceptibility to corrosion initiation for LAGBs for short immersion times. However, the number of corroded GBs was multiplied by 5.6, 3.8 and 3.3 for LAGBs, CSL HAGBs and RHAGBs, respectively, between 72hCI and 168hCI, which suggested an increase in the susceptibility to corrosion initiation for all GBs as the immersion time increased. Nevertheless the increase was higher for LAGBs than for CSL HAGBs and RHAGBs, whereas CSL HAGBs and RHAGBs seemed to retain a similar susceptibility to corrosion initiation for long immersion times. Similarly, for cyclic corrosion tests, the number of corroded GBs strongly increased for LAGBs as the number of cycles increased, whereas it remained constant for CSL HAGBs and RHAGBs in such a way as, for 3CR and 7CR tests, the number of corroded RHAGBs (and also CSL HAGBs) was significantly lower than the number of corroded LAGBs. Moreover, the number of corroded LAGBs was higher for cyclic corrosion tests compared to continuous immersion tests with similar immersion times, whereas the number of corroded RHAGBs (same result for CSL HAGBs) was higher for 1CR test compared to 8hCI test, but was then similar for cyclic corrosion tests and continuous immersion tests with similar immersion duration when the test duration increased. This showed that cyclic corrosion tests strongly sensibilised LAGBs to corrosion initiation, suggesting a strong contribution of LAGBs to the corrosion damage for these tests, whereas there was no significant effect of alternate immersion/emersion periods on the susceptibility to corrosion initiation of the RHAGBs and CSL HAGBs.

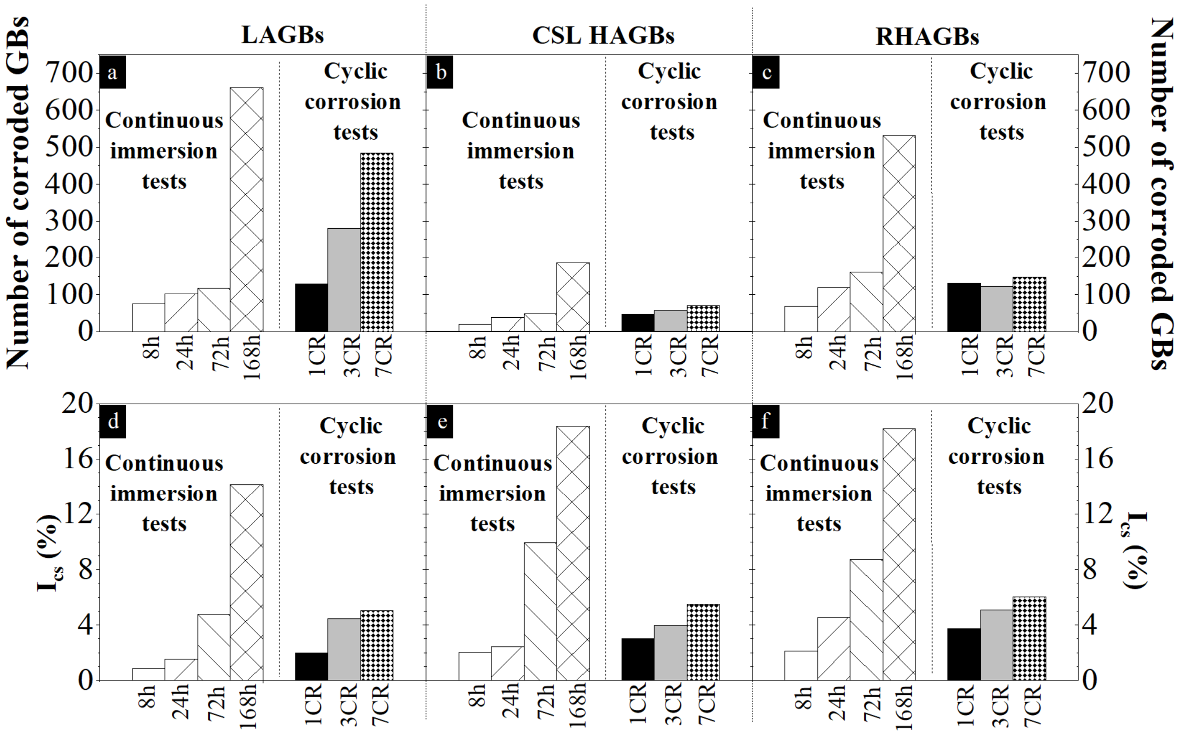

Fig. 6. Number of corroded GBs (a, b, c) and I_{cs} values (d, e, f) for corroded GBs of a given type after continuous immersion tests and cyclic corrosion tests. a) and d) LAGBs, b) and e) CSL HAGBs, c) and f) RHAGBs.

Attention was then given to corrosion propagation. Fig. 7 shows the total length of corroded GBs for each type of GBs, *i.e.* LAGBs, RHAGBs and CSL HAGBs, for continuous immersion tests and cyclic corrosion tests. First, regardless of the nature of the GBs, and for both continuous immersion tests and cyclic corrosion tests, the total length of corroded GBs increased when the immersion time increased, showing the global propagation of IGC defects when the immersion time increased. It was important to note here that, considering the previous results regarding initiation, the evolution of the total length of corroded GBs between two times, t_1 and t_2, included the propagation of IGC defects existing at t_1, and the initiation of new IGC defects between t_1 and t_2 followed by their propagation. This comment referred to the use of the terms “global propagation”. Then, for short immersion times (short continuous immersion tests, e.g. 8h, or cyclic corrosion test with only one cycle, *i.e.* 1CR test), the total length of corroded LAGBs was significantly lower than that of RHAGBs, whereas, for longer immersion times (long continuous immersion tests or cyclic tests with a large number of cycles), the total length of corroded LAGBs was quite similar (168h continuous immersion test) or even higher (7CR test) than that of corroded RHAGBs. This was in perfect agreement with the qualitative description of the corrosion damage (section 3.2, Fig. 5), with more branched defects for longer immersion times, confirming that, for short immersion times, the corrosion damage mainly concerned RHAGBs, but that, with increasing immersion time, the contribution of LAGBs was increasingly significant. Finally, regardless of the nature of the GBs, the total length of corroded GBs was higher for cyclic corrosion tests compared to continuous immersion tests with similar immersion time, *e.g.* 1CR (8h of immersion) compared to 8hCI or 3CR (3 x 8 = 24h of immersion) compared to 24hCI. For 7CR test, the total duration of the test was 168h (= 7x24), but the total duration of immersion was only 56h (=7x8). Therefore, the comparison should be made with the 72h continuous immersion test, even though, for this continuous immersion test, the duration of immersion was longer: the results showed that, except for RHAGBs, the total length of corroded GBs was longer after 7CR test than after 72h continuous immersion test. Then, it could even be observed that, for LAGBs, the total length of corroded GBs after a cyclic corrosion test was higher than after a continuous immersion test corresponding to an immersion time equal to the total duration of the cyclic corrosion tests (3CR test compared to 72hCI test). This was not true for RHAGBs and CSL HAGBs. This could be at least partly explained by the higher influence of alternate immersion/emersion periods on the susceptibility to corrosion initiation of LAGBs compared to HAGBs. That said, the results thus showed that cyclic corrosion tests accelerated the global propagation of IGC defects compared to continuous immersion tests regardless of the nature of the GBs; however, the influence of the exposure conditions was stronger for LAGBs compared to RHAGBs and CSL HAGBs, with the alternate immersion/emersion periods having a more deleterious effect on the global propagation of the corrosion damage at LAGBs. This was confirmed by the evolution of the total length of corroded GBs when the number of cycles increased: the total length of corroded RHAGBs and CSL HAGBs was multiplied by 1.75 and 2.4, respectively, between 1CR and 7CR tests, while it was multiplied by 4.7 for LAGBs. The same tendency was observed when the influence of the immersion time on the corrosion susceptibility of the GBs was quantified for continuous immersion tests: the total length of corroded RHAGBs and CSL HAGBs was multiplied by 7.6 and 8, respectively, between 8hCI and 168hCI tests, while it was multiplied by 13.5 for LAGBs. Therefore, the results confirmed that the influence of alternate immersion/emersion periods was more marked for LAGBs compared to RHAGBs when considering the global propagation of corrosion at a given type of GB. Moreover, considering these results and those obtained for the initiation step, it could be first concluded that the contribution of LAGBs to the corrosion damage was stronger for cyclic corrosion tests than for continuous immersion tests, even though it became of major importance for very long continuous immersion tests. Then, it could be also said that the contribution of LAGBs was quite similar to that of RHAGBs for very long continuous immersion tests, and even stronger for cyclic corrosion tests with a high number of cycles.

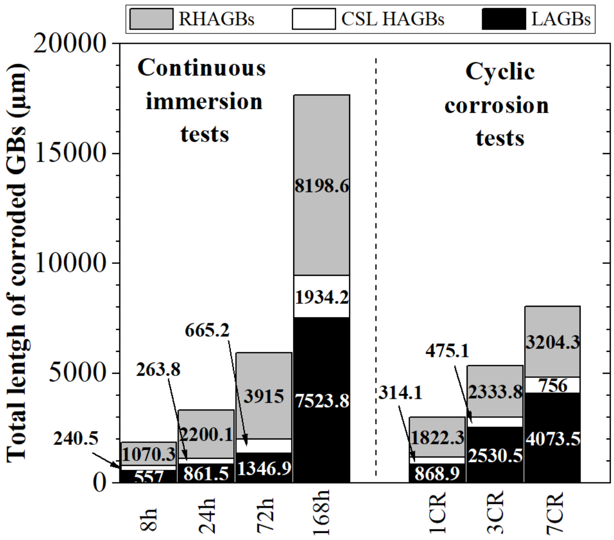

Fig. 7. *Total length of corroded GBs after continuous immersion tests and cyclic corrosion tests, for RHAGBs, CSL HAGBs and LAGBs for continuous immersion tests (8 h, 24 h, 72 h and 168 h) and cyclic corrosion tests (1CR, 3CR and 7CR) for 2024 Al alloy.*

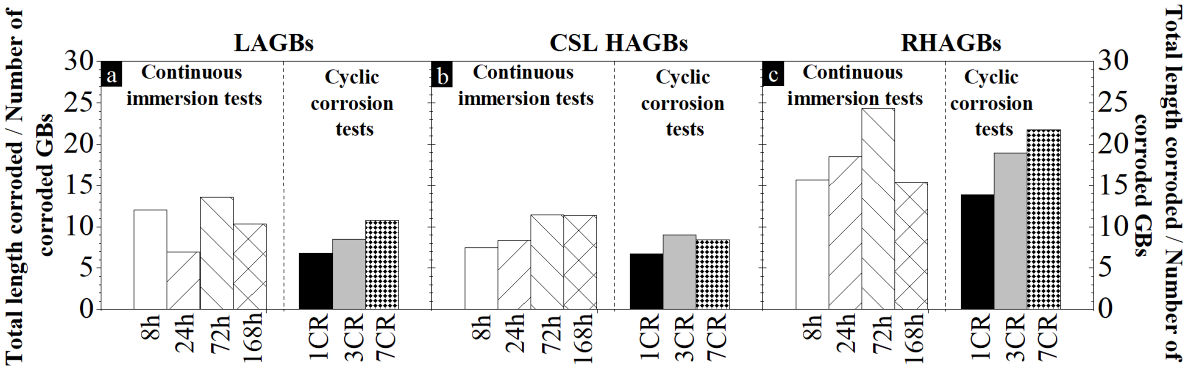

Fig. 8. *Ratio between the total length of corroded GBs and the number of corroded GBs for a given type of GB for continuous immersion tests (8 h, 24 h, 72 h and 168 h) and cyclic corrosion tests (1CR, 3CR and 7CR) for 2024 Al alloy. a) LAGBs, b) CSL HAGBs and c) RHAGBs.*

For a more accurate description of the kinetics of corrosion propagation, *i.e.* a more accurate evaluation of the susceptibility to corrosion propagation of the different types of GBs, we attempted to take into account the initiation of new IGC defects between two times t_1

and t_2. Therefore, the mean length of a corroded GB for the different exposure conditions was evaluated by calculating the ratio between the total length of corroded GBs and the number of corroded GBs for a given type of GB (Fig. 8). Globally, for all types of GBs, the results suggested an increase in the mean length of a corroded GB when the immersion time increased for continuous immersion tests, and when the number of cycles increased for cyclic corrosion tests. However, the tendency was not clear enough to allow further analysis of the susceptibility to corrosion propagation based on this approach. This was probably explained by considering that, even for a given type of GB, there was a large discrepancy in the corrosion behaviour of each GB. Such a comment could be related to the result obtained by Lacroix *et al.* [50] when studying the dissolution kinetics of S-phase particles; the authors showed that the dissolution kinetics of S-phase particles varied over a large range, even for similar chemical composition. This led us to conclude that the only way to study properly the susceptibility to corrosion propagation of a type of GB was to follow the extent of corrosion as a function of time for a selected GB. Of course, this had to be done for a large number of GBs, for each type of GBs, which would be strongly time-consuming. Therefore, in the following, the susceptibility to corrosion propagation was only analysed considering the concept of “global propagation” previously defined.

The evolution of the susceptibility to global corrosion propagation for the different types of GBs was then quantified by calculating I_{cs} value, as defined in section 2.3. Fig. 6 clearly showed that the increase in I_{cs} values was higher for LAGBs (Fig. 6d) compared to CSL HAGBs (Fig. 6e) and RHAGBs (Fig. 6f) when the immersion time increased for continuous immersion tests (from $I_{cs} = 1$ for 8hCI to $I_{cs} = 14$ for 168hCI for LAGBs compared to an evolution from $I_{cs} = 2$ for 8hCI to $I_{cs} = 18$ for 168hCI for RHAGBs), or when the number of cycles increased for cyclic corrosion tests (from $I_{cs} = 2$ for 1CR to $I_{cs} = 5$ for 7CR for LAGBs compared to an evolution from $I_{cs} = 4$ for 1CR to $I_{cs} = 6$ for 7CR for RHAGBs). This confirmed that the influence of the exposure conditions on global corrosion propagation was stronger for LAGBs compared to RHAGBs and CSL HAGBs. Furthermore, it could be observed that I_{cs} values for LAGBs were lower than for RHAGBs and CSL HAGBs when considering short continuous immersion tests and cyclic corrosion tests with a low number of cycles (1 cycle). However, for long continuous immersion tests and 7CR tests, I_{cs} values calculated for LAGBs remained lower than those for RHAGBs and CSL HAGBs, but became close to these values. It could be also noted that the differences in I_{cs} values between RHAGBs and CSL HAGBs for one part, and LAGBs for the other part, were more reduced after cyclic corrosion tests with a high number of cycles than after long continuous immersion tests. The results thus showed that the RHAGBs and CSL HAGBs were intrinsically more susceptible to global corrosion propagation than LAGBs; however, when the immersion time increased and/or when the number of cycles increased, all GBs achieved an equivalent susceptibility to global corrosion propagation, with cyclic corrosion tests promoting significantly the global corrosion propagation at LAGBs. It was of interest to note, at this point, that CSL HAGBs showed an intrinsic susceptibility to global corrosion propagation lower than RHAGBs, but the differences between both GBs were very low, and were not as high as expected from the literature that indicates that CSL HAGBs are less susceptible to corrosion than RHAGBs [3,15,16], except for the work of Bartawi *et al.* who showed that the corrosion susceptibility of CSL HAGBs could be close to that of RHAGBs [1]. The result obtained in the present study enabled us to conclude that CSL HAGBs are globally as susceptible to corrosion initiation and propagation as RHAGBs, in agreement with Bartawi *et al.* Their low contribution to IGC damage is mainly explained by the fact that they do not constitute a significant proportion in length of the cumulative length of GBs.

To complete the analysis, in particular to highlight the branching of the IGC defects, the corrosion susceptibility of the alloy was evaluated by considering the corroded areas defined as a network of corroded GBs all connected to each other (Fig. 2). Fig. 9 showed that the number of corroded areas increased when the immersion time increased for continuous immersion tests, whereas it decreased when the number of cycles increased for cyclic corrosion tests. The results were in perfect agreement with the previous analysis of the susceptibility to corrosion initiation and propagation of LAGBs and RHAGBs. Indeed, as said before, during continuous immersion tests, the extent of the corrosion damage proceeded by the propagation of existing corrosion defects and initiation of new corrosion defects. LAGBs had a slightly lower susceptibility to corrosion initiation than RHAGBs for short immersion times; furthermore, RHAGBs were more susceptible to global corrosion propagation, and, even though the difference in global corrosion propagation susceptibility decreased between LAGBs and RHAGBs when the immersion time increased, RHAGBs remained more susceptible to global corrosion propagation in such a way that IGC defects remained linear, even though a tendency to branching was observed for long immersion times due to the increase in the susceptibility to corrosion initiation and propagation of LAGBs. This led to the observation of increased number of corroded areas when the immersion time increased. On the contrary, for cyclic corrosion tests, LAGBs became as susceptible to global corrosion propagation as RHAGBs and were also more susceptible to corrosion initiation when the number of cycles increased. This led to the formation of highly branched IGC defects, and therefore a decrease in the number of corroded areas as the number of cycles increased. Those results were in perfect agreement with previous observations of the morphology of the IGC defects (Fig. 5). Finally, the results also showed that LAGBs and RHAGBs were the main contributors to the extent of the corrosion damage whatever the exposure conditions.

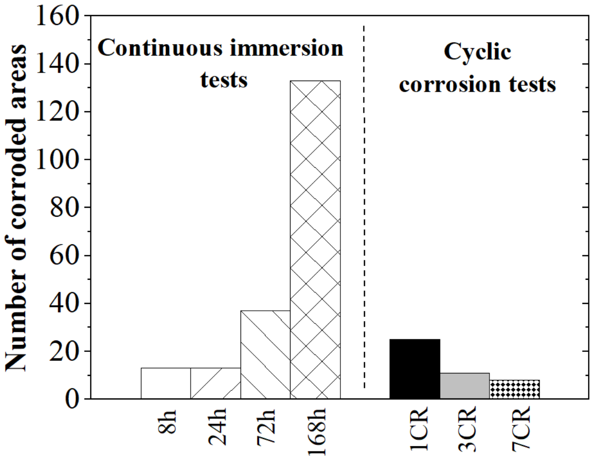

Fig. 9. *Number of corroded areas for the 2024 Al alloy after continuous immersion tests (8 h, 24 h, 72 h and 168 h) and cyclic corrosion tests (1CR, 3CR and 7CR).*

3.4. Evaluation of the influence of chloride ions concentration on the corrosion susceptibility of GBs

Literature data clearly showed that the concentration of chloride ions in the electrolyte trapped inside the IGC defects increased when the IGC defect propagated, *i.e.* when switching from a short IGC defect to a long IGC defect [31]. Similarly, the strong aggressiveness of cyclic corrosion tests compared to continuous immersion tests was partly explained by referring to the increase in chloride content of the trapped electrolyte due to the emersion period. The authors then proposed that this change in chloride concentration contributed to explain the evolution of the IGC defect morphology for long continuous immersion tests compared to short tests for one part, and for cyclic corrosion tests compared to continuous immersion tests for the other part [31,36]. The influence of chloride ion concentration on the susceptibility to corrosion initiation and global propagation of the different types of GBs was studied in the present study to go further in the understanding of the susceptibility to intergranular corrosion of the alloy: therefore, additional 24hCI tests were performed in 10 mM and 100 mM chloride solutions. The duration of the continuous immersion tests performed here, *i.e.* 24 h only, was chosen to generate mainly short IGC defects and avoid significant evolution in the chloride concentration of the electrolyte trapped inside the IGC defects. This allowed us to assume that the chloride concentration of the electrolyte trapped inside the IGC defects was that of the bulk solution.

Fig. 10 shows the number of corroded GBs for the 3 chloride concentrations, and for the 3 types of GBs. Results clearly showed that the increase in chloride content promoted corrosion initiation for all GBs; however, the impact was stronger for LAGBs (Fig. 10a), compared to CSL HAGBs (Fig. 10b) and RHAGBs (Fig. 10c), the number of corroded GBs being multiplied by 7.5, 4.5 and 4.2 for LAGBs, CSL HAGBs and RHGBs, respectively, as the chloride concentration was multiplied by 20 (from 5mM to 100 mM). Therefore, for high chloride concentrations, LAGBs were found to be more susceptible to corrosion initiation than RHAGBs and CSL HAGBs [49]. It could also be noted that the number of corroded CSL HAGBs was very low whatever the chloride concentration of the solution, as shown previously. This was explained by the low contribution of CSL HAGBs to the cumulative length of GBs, as concluded previously. Then, Fig 11 shows that the total length of corroded GBs increases for all types of GBs when the chloride concentration increases showing that chloride ions promote the propagation of all types of GBs. However, when the chloride ion concentration was multiplied by 20 (from 5 mM to 100 mM), the total length of corroded GBs was multiplied by 6.6, 3.9 and 1.7 for LAGBs, CSL HAGBs and RHAGBs, respectively. This showed that the increase in chloride content impacted more the global corrosion propagation of LAGBs compared to HAGBs. Considering the results regarding corrosion initiation and propagation, the consequence was that, for low chloride concentrations, RHAGBs were the major contributors to the corrosion damage. However, for high chloride concentrations, the corrosion damage was mostly related to LAGBs, without neglecting the contribution of

RHAGBs. This conclusion was confirmed by calculations of I_{cs} values for each type of GBs, with I_{cs} values multiplied by 6.8, 6 and 3 when the chloride concentration increased from 5 to 100 mM, for LAGBs, CSL HAGBs and RHAGBs, respectively. Furthermore, whatever the chloride concentration, RHAGBs were more susceptible to global corrosion propagation than LAGBs, but the difference in susceptibility was reduced when the chloride content increased, in agreement with the previous conclusion regarding the effect of increased chloride content on the susceptibility to global corrosion propagation of each type of GB. Finally, it could be also noted that I_{cs} values measured for CSL HAGBs were globally similar to those measured for the other GBs whatever the chloride concentration, leading us to conclude that the low contribution of CSL HAGBs to the corrosion damage was mainly explained by their low contribution to the cumulative length of GBs.

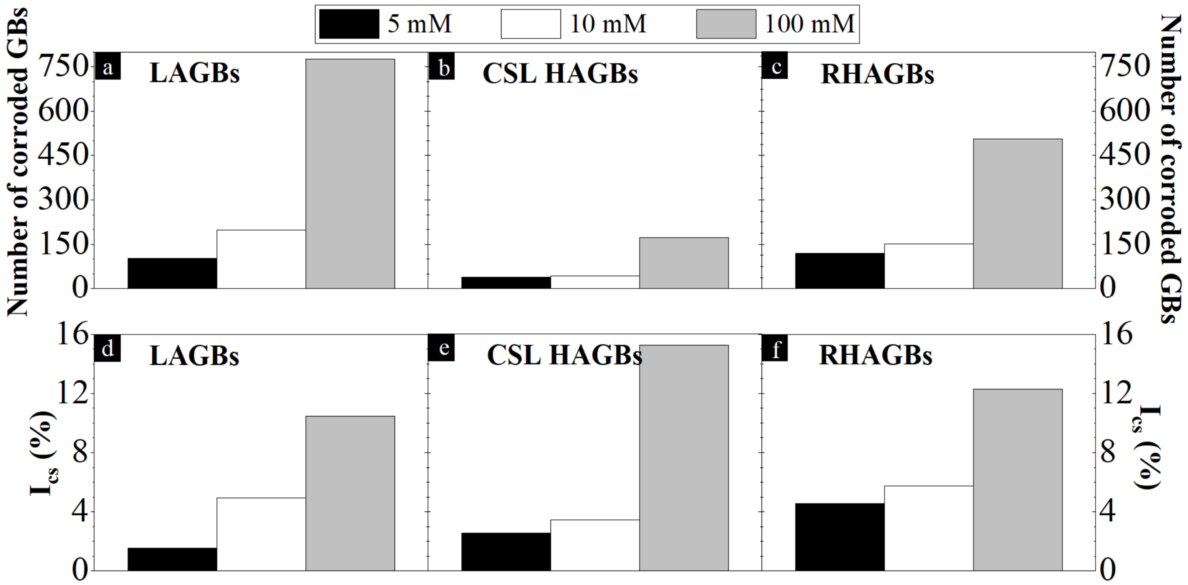

Fig. 10. *Number of corroded GBs and I_{cs} values for corroded GBs of a given type. a) and d) LAGBs, b) and e) CSL HAGBs, c) and f) RHAGBs. Results are given for 24h continuous immersions in 5 mM, 10 mM and 100 mM NaCl solutions.*

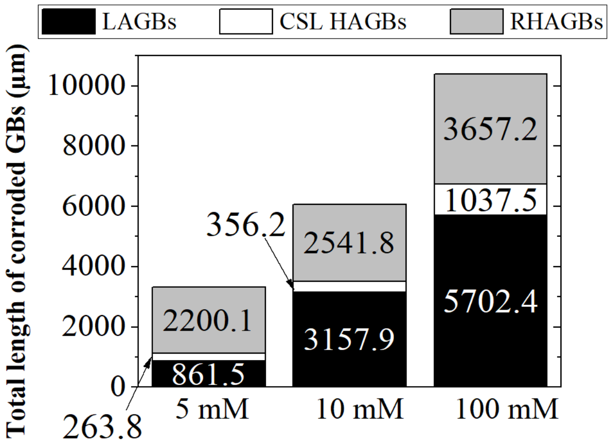

Fig. 11. *Total length of corroded GBs for 24h continuous immersions in 5 mM, 10 mM and 100 mM NaCl solutions for the 2024 Al alloy.*

These additional results confirmed that the evolution in chloride content of the electrolyte trapped inside the IGC defects when the immersion time was longer and for cyclic corrosion tests with a high number of cycles could explain, at least partially, the increased susceptibility to corrosion of LAGBs. Therefore, it could constitute a first order parameter to explain the change in corrosion morphology for long continuous immersion tests compared to short tests, and for cyclic corrosion tests compared to continuous immersion tests.

3.5. Focus on the influence of hydrogen on the corrosion susceptibility of GBs

We showed in previous studies that hydrogen increased the susceptibility to corrosion of the GBs, and strongly promoted the corrosion initiation at the LAGBs [10]. Furthermore, we also showed that the hydrogen uptake increased when the immersion time increased for continuous immersion tests, and was higher for cyclic corrosion tests compared to continuous immersion tests with similar duration of immersion. Therefore, hydrogen was also suspected to be a major parameter to explain the evolution in the corrosion morphology when the immersion time increased, and for cyclic corrosion tests compared to continuous immersion tests.

To go further in the evaluation of the influence of hydrogen on the corrosion susceptibility of the GBs, the global hydrogen content was measured for all corrosion tests. Fig. 12 first shows an hydrogen uptake for all corrosion tests. Moreover, the hydrogen content was found to increase with the duration of the continuous immersion, and reached 22 wppm for 168hCI tests, to be compared to 1.5 wppm for the non-corroded samples. Finally, it was of importance to note that the hydrogen content was significantly higher after cyclic tests, varying from 11 to 90 wppm after 1CR and 7CR tests, respectively. In other words, it could be noted that, for the same duration of immersion, *e.g.* 24h, the hydrogen content was 6 wppm and 42 wppm after 24hCI and 3CR tests, respectively, clearly showing that cyclic tests led to a significantly higher hydrogen uptake than continuous immersion tests.

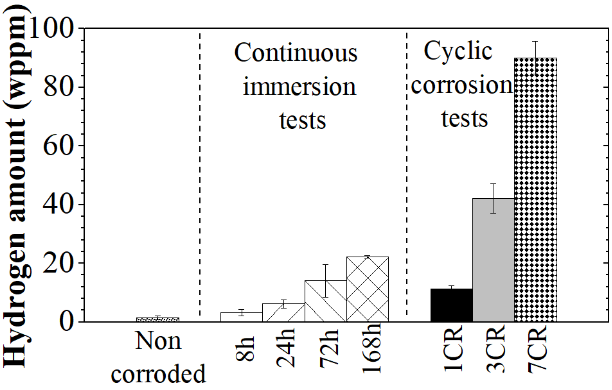

Fig. 12. *Hydrogen content measured for 2024 Al alloy. Results are given for non-corroded sample, after continuous immersion tests (8, 24 h, 72 h and 168 h) and after cyclic corrosion tests (1CR, 3CR and 7CR).*

Then, SKPFM surface maps were plotted to study the distribution of hydrogen at the polycrystal scale after a 24hCI test (Fig. 13b) and after a 1CR test (Fig. 13e and Fig. 14a). Several SKPFM maps were plotted for each sample in order to obtain consolidated results. In the following, only one map is presented after a 24hCI test and two maps are shown after 1CR test for brevity reasons, but the results are representative of all analyses performed. We demonstrated the interest of SKPFM for the detection of hydrogen in an aluminium alloy in previous works [45,51]. In particular, Larignon *et al.* clearly showed, by combining secondary ion mass spectrometry and SKPFM, that the potential contrast observed on SKPFM maps at the corroded GBs could not be attributed only to variations in the concentrations of alloying elements, e.g. copper or magnesium, but had to be related to hydrogen enrichment [51]. This was confirmed by Lafouresse *et al.* who showed changes in SKPFM maps when heat treatments were applied to induce hydrogen desorption [45]. Evers *et al.* have also shown SKPFM to be a powerful tool for detecting hydrogen, e.g. for palladium [52,53]; they postulated that the presence of hydrogen in the palladium lattice led to a correlated potential at the surface. For aluminium alloys, Oger *et al.* proposed that hydrogen could distort the metal lattice, leading to local relaxation of the subsurface and subsequent variation of the electronic work function [54]. In the present paper, for 24hCI test, comparison of the SEM observation of a corroded RHAGB (Fig. 13a) and the SKPFM map of the same zone (Fig. 13b) showed that hydrogen was produced at the HAGBs due to the corrosion processes, *i.e.* anodic dissolution followed by hydrolysis of the cations, and therefore the production of protons that finally reduce to lead to the hydrogen uptake [23,30,31]. However, hydrogen was only present at the corroded RHAGBs, and the potential profile plotted across the corroded GBs was narrow (Fig. 13c), showing low diffusion of hydrogen inside the surrounding matrix. On the contrary, after 1CR test, hydrogen was detected over a very large zone (Fig. 13e, f and Fig. 14a, e) all along the corroded RHAGBs. This confirmed a strong hydrogen diffusion from the RHAGB to the surrounding matrix. Furthermore, Fig. 13d clearly showed corroded LAGBs connected to the corroded RHAGBs. Those LAGBs were hidden in the hydrogen affected zone in the SKPFM map (Fig. 13e). These analyses therefore showed a significant difference in the hydrogen content and distribution between 24hCI and 1CR tests, which could contribute to explain the increase in the susceptibility to corrosion initiation and propagation of LAGBs during cyclic corrosion tests. It may be mentioned here that the presence of hydrogen in the matrix surrounding the corroded GBs had to be linked to the diffusion of hydrogen in atomic form. Nevertheless, the presence of hydrogen in the form of hydrogen molecules in corroded GBs could not be neglected, as postulated by Bonfils *et al.* who observed flaws in corroded GBs when they characterised the IGC defects by transmission electron microscopy [18].

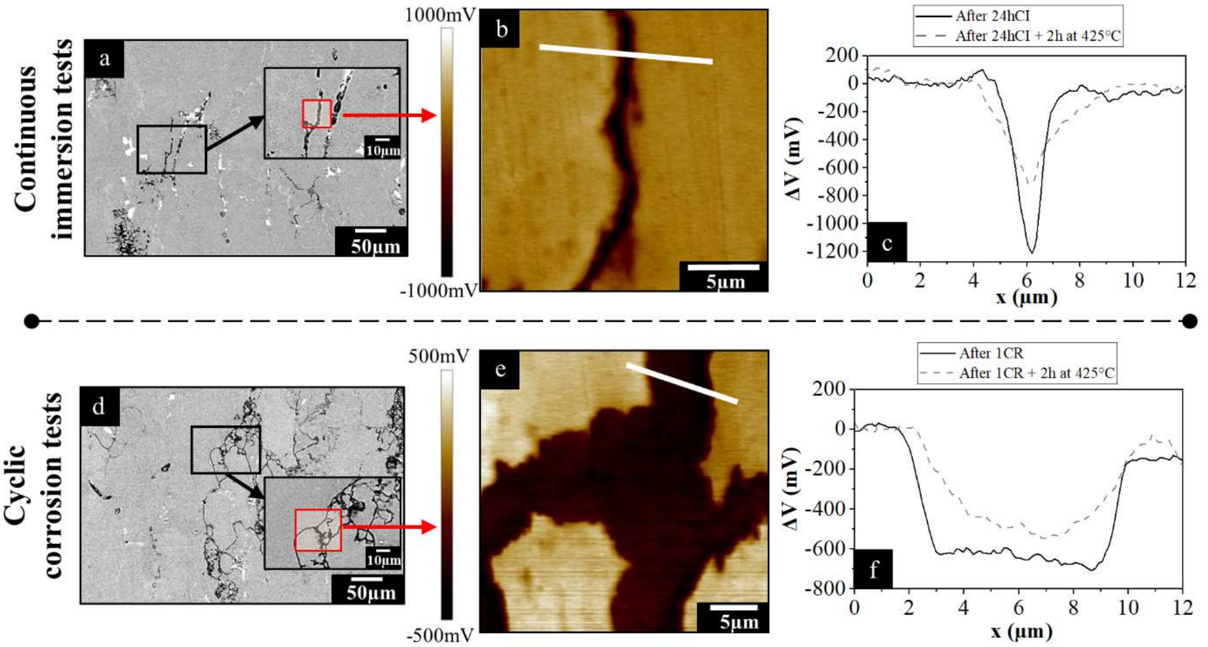

Fig. 13. *SKPFM analysis of corroded 2024 Al alloy a) and d) SEM images, b) and e) SKPFM maps, c) and f) Volta potential profiles obtained after 24h continuous immersion test (a, b, c) and after 1CR test (d, e, f).*

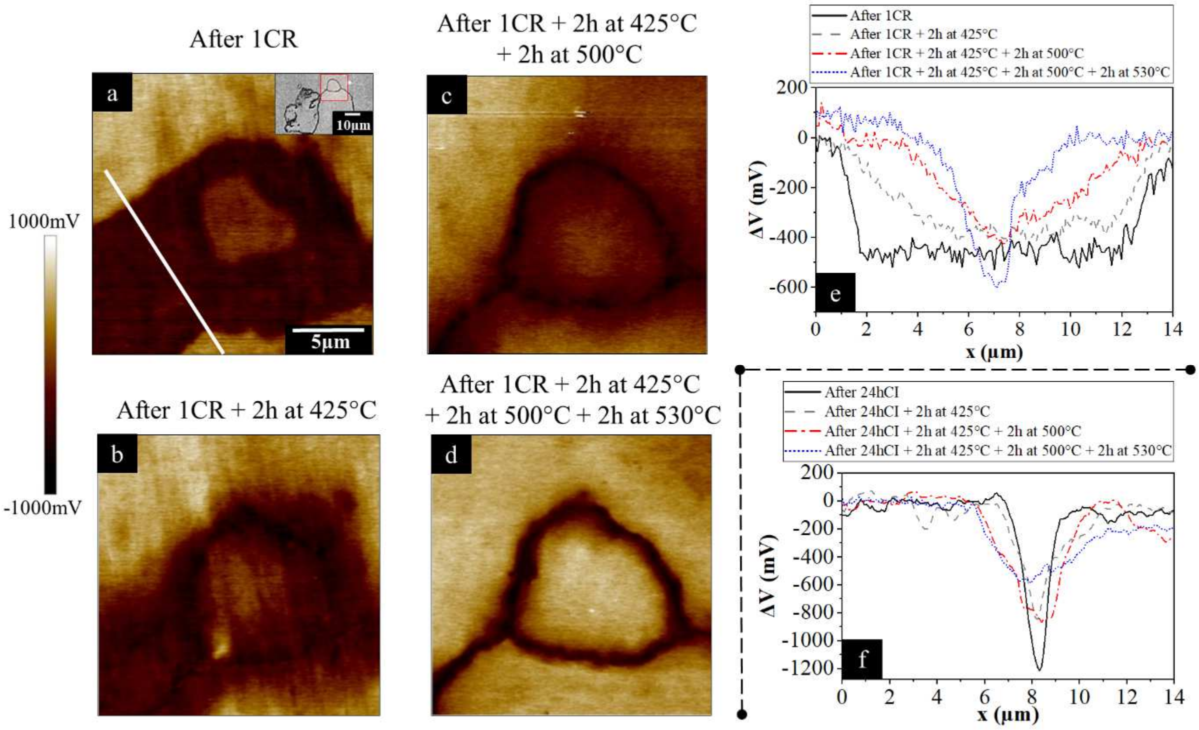

Fig. 14*. SKPFM analysis of corroded 2024 Al alloy. SKPFM maps plotted after a) 1CR test, b) 1 CR test followed by a 2h heat treatment at 425°C, c) 1 CR test followed by two heat treatments (2h at 425°C + 2h at 500°C), d) 1 CR test followed three heat treatments (2h at 425°C + 2h at 500°C + 2h at 530°C). SEM image of the corroded sample is shown in the insert of a). e) Volta potential profiles corresponding to SKPFM maps shown in a) –d). f) Volta potential profiles plotted after 24hCI test (SKPFM map shown in Fig. 13b) and after different heat treatments are also given for comparison: Volta potential profiles plotted immediately after 24h CI test and after an additional 2h heat treatment at 425°C are those given in Fig. 13 c).*

To go further in the analysis of the role of hydrogen on corrosion kinetics, desorption treatments were first performed at 425 °C for 2 h. Considering literature data, this temperature was assumed to be high enough to allow hydrogen detrapping from low-energy traps and, at least, some of the highest-energy traps [55-57]. Results (Fig. 13 c, f) clearly showed a decrease in the potential signal attributed to hydrogen for both 24hCI and 1CR samples after desorption treatment, but the signal remained high for the two samples, suggesting hydrogen trapping at different sites, in particular deep trapping sites, during the corrosion tests. TDS analyses were therefore performed to identify the hydrogen traps depending on the exposure conditions. Fig. 15a is an example of a TDS spectrum plotted for the 3CR sample. Similar spectra were obtained for the 24hCI and 72hCI samples. They showed four desorption peaks, referred to as P1 to P4, and corresponding to desorption temperatures of 330, 390, 455 and 510 °C, respectively. These values were in perfect agreement with literature data [58], even though some differences in the desorption temperatures were observed, which could be explained by referring to the influence of the sample thickness and heating rate. Each of the four peaks could be considered to be associated with a particular trapping site characterised by a trapping energy. For 7xxx Al alloys, Scully *et al.* showed that dislocations, the distorted lattice, Mg in solid solution and η precipitates could be identified as hydrogen trapping sites, even if uncertainties could exist in attributing a peak to a specific microstructural feature [58]. For 2024 Al alloy, Kamoutsi *et al.* identifed four trapping sites with increasing desorption energies: the first peak was attributed to lattice sites, the second to the stress fields of coherent GPB zones and S'' phase, the third to dislocations and the fourth to strengthening θ and/or S phase [56,57,59]. In the present work, in agreement with Kamoutsi *et al.*, peak P1 was associated with lattice hydrogen, peak P2 with hydrogen trapped by the stress fields of coherent GPB zones, and peak P3 with dislocations. However, based on Oudriss' work [60], a distinction was made between hydrogen trapped in the elastic field and in the core of dislocations (deep trapping), corresponding to peaks P3 and P4, respectively. Then, referring to the microstructure of the 2024 Al alloy, it was assumed that P3 and P4 peaks were characteristic of the hydrogen trapped at LAGBs, commonly described as a dislocation network [61]. Concerning HAGBs, they are commonly identified as short circuit of diffusion; in that sense, hydrogen present at HAGBs was rapidly desorbed during TDS analyses in such a way that it was not possible to distinguish between lattice hydrogen and hydrogen present at HAGBs in the limit of the experiments performed here. Fig. 15b showed that the total ratios of hydrogen trapped in P1 and P2 traps (about 55 %) for the one hand, and in P3 and P4 traps (about 45 %) for the other hand, were similar for the three corroded samples. Moreover, no significant difference in the ratio of hydrogen trapped in P1 and P2 traps was observed between the three corroded samples, with ratio of hydrogen trapped in P1 and P2 traps of about 25 % and 30 %, respectively, whatever the samples. However, it was of major interest to note that the ratios of hydrogen trapped in P3 and P4 traps were 34 (31) % and 15 (11) %, respectively for 24hCI (72hCI) samples, while they were equal to 19 % and 26 % for 3CR samples: this showed that, after continuous immersion tests, most part of the hydrogen trapped at LAGBs was trapped in the elastic field of the dislocations, while hydrogen was mostly deeply trapped in the core of the dislocations after cyclic tests. This also meant that hydrogen trapped at LAGBs was spatially distributed over a long-range stress field associated with dislocations after continuous immersion tests, whereas it was concentrated in a much more reduced volume (core of dislocations) after cyclic tests. Keeping also in mind that the global hydrogen amount was higher after cyclic tests compared to continuous immersion tests, it seemed relevant to assume that, at the atomic scale, the amount of hydrogen trapped at LAGBs after cyclic tests was significantly higher than after continuous immersion tests, leading to a stronger modification of the chemical potential of the metallic atoms [62], and therefore enhancing the susceptibility to dissolution of LAGBs.

Finally, it was of interest to note that a progressive change was observed on the SKPFM maps (Fig. 14 a-d) when desorption heat treatments were performed at increasing temperatures (425°C, 500°C and 530°C to desorb hydrogen trapped in sites P1 and P2, in sites P1, P2 and P3, and in all sites, respectively), confirming, on the one hand, that the potential contrast had to be related to hydrogen, and, on the other hand, the existence of different hydrogen trapping sites. Furthermore, comparison of the Volta potential profiles plotted after the various desorption treatments for 1CR sample (Fig. 14 e) and for 24hCI sample (Fig. 14f) showed that the Volta potential contrast decreased progressively for 24hCI sample, whereas it remained high for 1CR sample, confirming that a greater part of hydrogen was deeply trapped for 1CR sample.

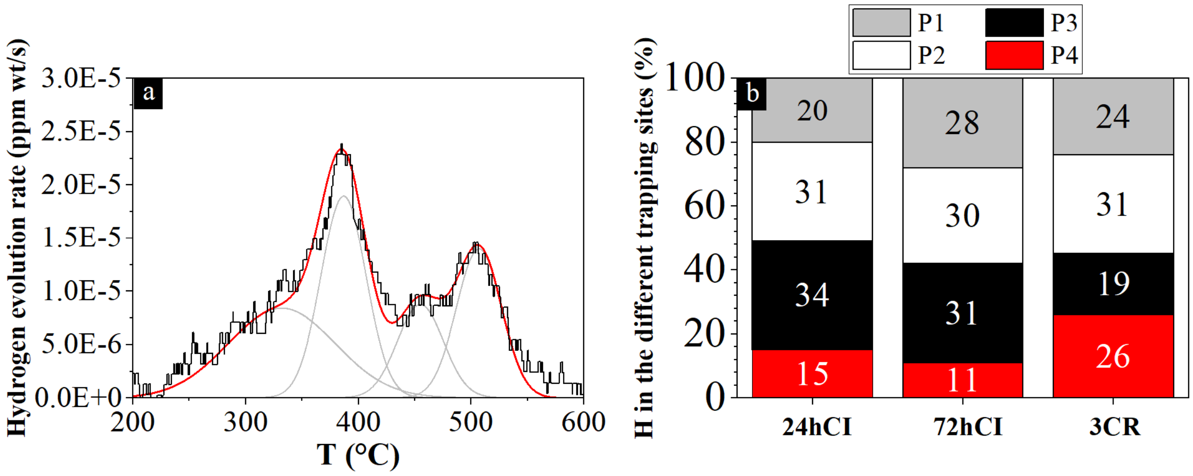

Fig. 15. *TDS analysis of corroded 2024 Al alloy a) TDS spectrum plotted after a 3CR test, b) total ratios of hydrogen trapped in P1 to P4 traps for continuous immersion tests (24 h and 72 h) and cyclic corrosion test (3CR).*

Combining all the results presented above, it therefore seemed possible to propose consolidated hypotheses to explain why the GBs had different susceptibilities in continuous immersion tests and cyclic corrosion tests with the same immersion time. First, Larignon *et al.* clearly showed that the chloride concentration of the electrolyte trapped inside the IGC defects could reach values as high as 5M during cyclic corrosion tests, *i.e.*, higher values than those reached during continuous immersion tests due to the evaporation of the electrolyte during the emersion period [31]. Taking into account the influence of chloride concentration on the IGC susceptibility of the GBs (section 3.4), this could contribute to explain the higher

IGC susceptibility of the GBs for cyclic corrosion tests compared to continuous immersion tests for a similar immersion time. Furthermore, Bonfils *et al.* demonstrated that hydrogen enhanced the kinetics of anodic dissolution [10,63]. Therefore, the higher hydrogen uptake observed for cyclic corrosion tests compared to continuous immersion tests could also contribute to explain the results. More specifically, the higher IGC susceptibility of the GBs for cyclic corrosion tests compared with continuous immersion tests for a similar immersion time, particularly that of LAGBs, could be explained considering that, at the atomic scale, the amount of hydrogen trapped at the LAGBs was higher after cyclic corrosion tests than after continuous immersion tests, as shown by the TDS results (Fig. 15). Nevertheless, bearing in mind that hydrogen was produced by the corrosion processes, it seemed relevant to consider IGC as an autocatalytic process. As IGC defects propagated, the chloride ion concentration of the electrolyte trapped within the IGC defects increased, leading to an increase in the corrosion processes and hydrogen production, and the hydrogen itself then promoted the corrosion processes. In this sense, it was difficult to distinguish the contribution of the chloride ion concentration from that of hydrogen on the IGC susceptibility of the GBs. An intricate interplay between these two parameters should be considered.

Finally, in this paper, the IGC susceptibility of 2024 Al alloy was studied by measuring the lateral extension in the surface plane (LT-ST), and depth penetration was not analysed. However, Larignon *et al.* performed observations for a 2024 Al alloy exposed to similar corrosion tests and measured the size of IGC defects in the L-ST plane, in particular the depth of IGC defects in the L direction [31]. Their results led to similar conclusions, with cyclic corrosion tests being more aggressive than continuous immersion tests and leading to more branched defects due to the increase in IGC susceptibility of LAGBs with cyclic corrosion tests. However, microstructure gradients are often observed perpendicularly to the rolling plane for thick rolled plates; this was the case in this paper, as indicated in the experimental section with recrystallised grains near the rolling plane and elongated grains in the rolling direction in the core of the plate. Furthermore, the variation in precipitation state at the GBs can also be observed with depth due to differences in cooling rate with depth during the water quench following the solution heat treatment [64]. The variation of GB crystallography and precipitation state with depth, as well as the stress state, could significantly influence the results.

4. Conclusions

This paper provides a new insight into the understanding of the susceptibility to IGC of 2024 Al alloy, clarifying the influence of the exposure conditions, in particular the role of corrosion-induced hydrogen, on the susceptibility to initiation and propagation of LAGBs, CSL HAGBs and RHAGBs. The major conclusions are as follows:

1. For continuous immersion tests, all GBs showed similar susceptibility to corrosion initiation, whereas cyclic corrosion tests increased the susceptibility to corrosion initiation of LAGBs, which was not the case for RHAGBs and CSL HAGBs.

2. RHAGBs and CSL HAGBs showed similar susceptibility to corrosion propagation, and were intrinsically more susceptible to global corrosion propagation than LAGBs. However, cyclic corrosion tests significantly promoted the global corrosion propagation at LAGBs.

3. Whatever the exposure conditions, LAGBs and RHAGBs were the main contributors to the extent of the IGC damage because CSL HAGBs represent only a small proportion of GBs. Furthermore, whatever the types of GBs, cyclic corrosion tests promoted the global propagation of IGC defects compared to continuous immersion tests, but the effect was stronger for LAGBs compared to RHAGBs and CSL HAGBs, in such a way that cyclic tests

led to more extended IGC damage, with more branched IGC defects, than continuous immersion tests.

4. The chloride concentration was identified as a first order parameter to explain the IGC damage. Whatever the chloride concentration, RHAGBs were more susceptible to global corrosion propagation than LAGBs. An increase in chloride content promoted both corrosion initiation and propagation for all GBs, but the effect was stronger for LAGBs, contributing to explain the higher contribution to the IGC damage of LAGBs for cyclic tests.
5. Corrosion-induced hydrogen was identified as another critical parameter controlling the IGC damage. Hydrogen was deeply trapped in the core of the dislocations defining LAGBs after cyclic corrosion tests, which could contribute to explain the enhanced susceptibility to corrosion initiation and propagation of LAGBs after cyclic corrosion tests.

In view of the literature review proposed in the introduction, it seems appropriate to propose that some of the conclusions obtained here for 2024 Al alloy may apply to other relatively similar alloys, in particular alloys of the 2000 series. Nevertheless, caution is required before generalising all the results to these alloys, or even to alloys with very different microstructures. In particular, hydrogen/microstructure interactions are very complex and must be analysed with caution.

Acknowledgments

This work was financially supported by le Ministère des armées - Agence de l'Innovation de Défense. The authors thank Abdelali Oudriss for fruitful discussions about TDS analyses.

Data availability

The raw/processed data required to reproduce these findings cannot be shared at this time as the data also forms part of an ongoing study.

Credit authorship contribution statement

E. Mondou: Investigation, Formal analysis, Validation, Visualization, Methodology, Data curation, Writing - original draft, Writing - review & editing. **A. Proietti**: Investigation for EBSD experiments, Formal analysis for EBSD experiments, Validation for EBSD experiments, Writing - review & editing. **C. Charvillat**: Investigation for SKPFM experiments, Formal analysis for SKPFM experiments, Validation for SKPFM experiments, Writing - review & editing. **C. Berziou**: Investigation for TDS experiments, Formal analysis for TDS experiments. **X. Feaugas**: Methodology for TDS experiments, Formal analysis for TDS experiments, Validation for TDS experiments, Writing -review & editing. **D. Sinopoli**: Funding acquisition, Project administration, Supervision, Validation, Writing -review & editing **C. Blanc**: Funding acquisition, Methodology, Formal analysis, Project administration, Supervision, Validation, Conceptualization, Data curation, Writing - original draft, Writing - review & editing.

References

[1] E.H. Bartawi, O.V. Mishin, G. Shaban, J.H. Nordlien, R. Ambat, Electron microscopy analysis of grain boundaries and intergranular corrosion in aged Al-Mg-Si alloy doped with 0.05 wt% Cu, Corros. Sci. 209 (2022) 110758. https://doi.org/10.1016/j.corsci.2022.110758.

[2] Y. Zhao, S. Niverty, X. Ma, N. Chawla, Correlation between corrosion behavior and grain boundary characteristics of a 6061 Al alloy by lab-scale X-ray diffraction contrast tomography (DCT), Mater. Charact. 193 (2022) 112325. https://doi.org/10.1016/j.matchar.2022.112325.

[3] B. Shang, L. Lei, X. Wang, P. He, X. Yuan, W. Dai, J. Li, Y. Jiang, Y. Sun, Effects of grain boundary characteristics changing with cold rolling deformation on intergranular corrosion resistance of 443 ultra-pure ferritic stainless steel, Corros. Commun. 8 (2022) 27–39. https://doi.org/10.1016/j.corcom.2022.07.002.

[4] S. Quan, R. Song, S. Su, Y. Huang, C. Cai, Y. Wang, K. Wang, Grain boundary engineering prepared by iterative thermomechanical processing of nickel-saving austenitic stainless steel: Excellent corrosion resistance and mechanical properties, Mater. Charact. 196 (2023) 112601. https://doi.org/10.1016/j.matchar.2022.112601.

[5] H. Hu, M. Zhao, S. Chen, L. Rong, Effect of grain boundary character distribution on hydrogen embrittlement in Fe–Ni based alloy, Mater. Sci. Eng. A. 780 (2020) 139201. https://doi.org/10.1016/j.msea.2020.139201.

[6] J.P. Hanson, A. Bagri, J. Lind, P. Kenesei, R.M. Suter, S. Gradečak, M.J. Demkowicz, Crystallographic character of grain boundaries resistant to hydrogen-assisted fracture in Ni-base alloy 725, Nat. Commun. 9 (2018) 3386. https://doi.org/10.1038/s41467-018-05549-y.

[7] S. Kobayashi, R. Kobayashi, T. Watanabe, Control of grain boundary connectivity based on fractal analysis for improvement of intergranular corrosion resistance in SUS316L

austenitic stainless steel, Acta Mater. 102 (2016) 397–405. https://doi.org/10.1016/j.actamat.2015.08.075.

[8] Y. Yuan, Y. Jiang, J. Zhou, G. Liu, X. Ren, Influence of grain boundary character distribution and random high angle grain boundaries networks on intergranular corrosion in high purity copper, Mater. Lett. 253 (2019) 424–426. https://doi.org/10.1016/j.matlet.2019.07.125.

[9] W. Feng, Z. Wang, Q. Sun, Y. He, Y. Sun, Effect of thermomechanical processing via rotary swaging on grain boundary character distribution and intergranular corrosion in 304 austenitic stainless steel, J. Mater. Res. Technol. 19 (2022) 2470–2482. https://doi.org/10.1016/j.jmrt.2022.06.032.

[10] M.-L. de Bonfils-Lahovary, C. Josse, L. Laffont, C. Blanc, Influence of hydrogen on the propagation of intergranular corrosion defects in 2024 aluminium alloy, Corros. Sci. 148 (2019) 198–205. https://doi.org/10.1016/j.corsci.2018.12.019.

[11] M. Guérin, J. Alexis, E. Andrieu, L. Laffont, W. Lefebvre, G. Odemer, C. Blanc, Identification of the metallurgical parameters explaining the corrosion susceptibility in a 2050 aluminium alloy, Corros. Sci. 102 (2016) 291–300. https://doi.org/10.1016/j.corsci.2015.10.020.

[12] S.-P. Tsai, P. Konijnenberg, S. Zaefferer, N. Peter, B. Gault, K. Kawano-Miyata, D. An, T.A. Griffiths, Correlative Microscopy Observation (3D EBSD + APT + TEM) on Intergranular Corrosion Behaviors in 316L Stainless Steel, Microsc. Microanal. 25 (2019) 748–749. https://doi.org/10.1017/S1431927619004471.

[13] Z. Ma, J. Liu, S. Liu, Y. Zhang, Y. Deng, Quench-induced contributions of high angle grain boundary and low angle grain boundary to exfoliation corrosion propagation in an AlZnMgCu alloy, J. Mater. Res. Technol. 15 (2021) 6866–6870. https://doi.org/10.1016/j.jmrt.2021.11.115.

[14] J. Zhang, L. Xu, Y. Han, L. Zhao, B. Xiao, New perspectives on the grain boundary misorientation angle dependent intergranular corrosion of polycrystalline nickel-based 625 alloy, Corros. Sci. 172 (2020) 108718. https://doi.org/10.1016/j.corsci.2020.108718.

[15] S.H. Kim, U. Erb, K.T. Aust, G. Palumbo, Grain boundary character distribution and intergranular corrosion behavior in high purity aluminum, Scr. Mater. 44 (2001) 835–839. https://doi.org/10.1016/S1359-6462(00)00682-5.

[16] S.H. Kim, U. Erb, K.T. Aust, G. Palumbo, Effect of Texture on the Corrosion Behaviour of High Purity Aluminum, Mater. Sci. Forum. 408–412 (2002) 1043–1048. https://doi.org/10.4028/www.scientific.net/MSF.408-412.1043.

[17] J.R. Galvele, S.M. De Micheli, Mechanism of intergranular corrosion of Al-Cu alloys, Corros. Sci. 10 (1970) 795–807.

[18] M.-L. de Bonfils-Lahovary, L. Laffont, C. Blanc, Characterization of intergranular corrosion defects in a 2024 T351 aluminium alloy, Corros. Sci. 119 (2017) 60–67. https://doi.org/10.1016/j.corsci.2017.02.020.

[19] X. Xiao, Z. Zhou, C. Liu, L. Cao, Microstructure and Its Effect on the Intergranular Corrosion Properties of 2024-T3 Aluminum Alloy, Crystals. 12 (2022) 395. https://doi.org/10.3390/cryst12030395.

[20] P. Campestrini, E.P.M. van Westing, H.W. van Rooijen, J.H.W. de Wit, Relation between microstructural aspects of AA2024 and its corrosion behaviour investigated using AFM scanning potential technique, Corros. Sci. 42 (2000) 1853–1861. https://doi.org/10.1016/S0010-938X(00)00002-0.

[21] C. Luo, X. Zhou, G.E. Thompson, A.E. Hughes, Observations of intergranular corrosion in AA2024-T351: The influence of grain stored energy, Corros. Sci. 61 (2012) 35–44. https://doi.org/10.1016/j.corsci.2012.04.005.

[22] Y. Ma, X. Zhou, Y. Liao, Y. Yi, H. Wu, Z. Wang, W. Huang, Localised corrosion in AA 2099-T83 aluminium-lithium alloy: The role of grain orientation, Corros. Sci. 107 (2016) 41–48. https://doi.org/10.1016/j.corsci.2016.02.018.

[23] A.M. Glenn, T.H. Muster, C. Luo, X. Zhou, G.E. Thompson, A. Boag, A.E. Hughes, Corrosion of AA2024-T3 Part III: Propagation, Corros. Sci. 53 (2011) 40–50. https://doi.org/10.1016/j.corsci.2010.09.035.

[24] V. Guillaumin, G. Mankowski, Localized corrosion of 2024 T351 aluminium alloy in chloride media, Corros. Sci. 41 (1998) 421–438. https://doi.org/10.1016/S0010-938X(98)00116-4.

[25] X. Zhou, C. Luo, Y. Ma, T. Hashimoto, G.E. Thompson, A.E. Hughes, P. Skeldon, Grain-stored energy and the propagation of intergranular corrosion in AA2xxx aluminium alloys: Grain-stored energy and the propagation of IGC, Surf. Interface Anal. 45 (2013) 1543–1547. https://doi.org/10.1002/sia.5218.

[26] M. Orłowska, E. Ura-Bińczyk, L. Olejnik, M. Lewandowska, The effect of grain size and grain boundary misorientation on the corrosion resistance of commercially pure aluminium, Corros. Sci. 148 (2019) 57–70. https://doi.org/10.1016/j.corsci.2018.11.035.

[27] R. Zhang, Y. Qiu, Y. Qi, N. Birbilis, A closer inspection of a grain boundary immune to intergranular corrosion in a sensitised Al-Mg alloy, Corros. Sci. 133 (2018) 1–5. https://doi.org/10.1016/j.corsci.2018.01.009.

[28] Q. Ding, D. Zhang, J. Zuo, S. Hou, L. Zhuang, J. Zhang, The effect of grain boundary character evolution on the intergranular corrosion behavior of advanced Al-Mg-3wt%Zn alloy with Mg variation, Mater. Charact. 146 (2018) 47–54. https://doi.org/10.1016/j.matchar.2018.09.044.

[29] F. Wen, J. Chen, S. Han, J. Ye, J. Ren, Y. Zhang, W. Li, R. Guan, The initial corrosion behavior of Al–Cu–Li bicrystals: effect of misorientation and precipitates, J. Mater. Res. Technol. 18 (2022) 3716–3724. https://doi.org/10.1016/j.jmrt.2022.04.024.

[30] Sp.G. Pantelakis, P.G. Daglaras, Ch.Alk. Apostolopoulos, Tensile and energy density properties of 2024, 6013, 8090 and 2091 aircraft aluminum alloy after corrosion exposure, Theor. Appl. Fract. Mech. 33 (2000) 117–134. https://doi.org/10.1016/S0167-8442(00)00007-0.

[31] C. Larignon, J. Alexis, E. Andrieu, C. Blanc, G. Odemer, J.-C. Salabura, Corrosion Damages Induced by Cyclic Exposure of 2024 Aluminum Alloy in Chloride-Containing Environments, J. Electrochem. Soc. 158 (2011) C284. https://doi.org/10.1149/1.3610401.

[32] C. Larignon, J. Alexis, E. Andrieu, G. Odemer, C. Blanc, Propagation of Intergranular Corrosion Defects in AA 2024-T351 Evaluated by a Decrease in Mechanical Resistance, J. Electrochem. Soc. 161 (2014) C339–C348. https://doi.org/10.1149/2.090406jes.

[33] M. Guérin, E. Andrieu, G. Odemer, J. Alexis, C. Blanc, Effect of varying conditions of exposure to an aggressive medium on the corrosion behavior of the 2050 Al–Cu–Li alloy, Corros. Sci. 85 (2014) 455–470. https://doi.org/10.1016/j.corsci.2014.04.042.

[34] A.P. Yadav, A. Nishikata, T. Tsuru, Electrochemical impedance study on galvanized steel corrosion under cyclic wet–dry conditions—influence of time of wetness, Corros. Sci. 46 (2004) 169–181. https://doi.org/10.1016/S0010-938X(03)00130-6.

[35] M.-C. Zhao, P. Schmutz, S. Brunner, M. Liu, G. Song, A. Atrens, An exploratory study of the corrosion of Mg alloys during interrupted salt spray testing, Corros. Sci. 51 (2009) 1277–1292. https://doi.org/10.1016/j.corsci.2009.03.014.

[36] R. Vera, D. Delgado, B.M. Rosales, Effect of atmospheric pollutants on the corrosion of high power electrical conductors: Part 1. Aluminium and AA6201 alloy, Corros. Sci. 48 (2006) 2882–2900. https://doi.org/10.1016/j.corsci.2005.11.012.

[37] N.D. Alexopoulos, C. Charalampidou, P. Skarvelis, S.K. Kourkoulis, Synergy of corrosion-induced micro-cracking and hydrogen embrittlement on the structural integrity of aluminium alloy (Al-Cu-Mg) 2024, Corros. Sci. 121 (2017) 32–42. https://doi.org/10.1016/j.corsci.2017.03.001.

[38] M. Winning, A.D. Rollett, Transition between low and high angle grain boundaries, Acta Mater. 53 (2005) 2901–2907. https://doi.org/10.1016/j.actamat.2005.03.005.

[39] P.L. Niu, W.Y. Li, N. Li, Y.X. Xu, D.L. Chen, Exfoliation corrosion of friction stir welded dissimilar 2024-to-7075 aluminum alloys, Mater. Charact. 147 (2019) 93–100. https://doi.org/10.1016/j.matchar.2018.11.002.

[40] A. Ingle, S. Heurtault, F. Hafid, J. Said, A. Proietti, G. Odemer, M. Dehmas, C. Blanc, Identification of the critical microstructural parameters on the corrosion behaviour of commercially pure aluminium alloy, Corros. Sci. 208 (2022) 110654. https://doi.org/10.1016/j.corsci.2022.110654.

[41] D.G. Brandon, The structure of high-angle grain boundaries, Acta Metall. 14 (1966) 1479–1484. https://doi.org/10.1016/0001-6160(66)90168-4.

[42] S. Oda, S.-I. Tanaka, Grain boundaries with high Σ value and strain in grain matrix induce crack initiation in extruded 6000 series aluminium alloys, Mater. Sci. Eng. A. 834 (2022) 142630. https://doi.org/10.1016/j.msea.2022.142630.

[43] W. Wang, C. Cai, G.S. Rohrer, X. Gu, Y. Lin, S. Chen, P. Dai, Grain boundary inter-connections in polycrystalline aluminum with random orientation, Mater. Charact. 144 (2018) 411–423. https://doi.org/10.1016/j.matchar.2018.07.040.

[44] Z.X. Ma, X.L. Xiong, L.N. Zhang, Z.H. Zhang, Y. Yan, Y.J. Su, Experimental study on the diffusion of hydrogen along individual grain boundaries in nickel, Electrochem. Commun. 92 (2018) 24–28. https://doi.org/10.1016/j.elecom.2018.05.012.

[45] M.C. Lafouresse, M.-L. de Bonfils-Lahovary, C. Charvillat, L. Oger, L. Laffont, C. Blanc, A Kelvin probe force microscopy study of hydrogen insertion and desorption into 2024 aluminum alloy, J. Alloys Compd. 722 (2017) 760–766. https://doi.org/10.1016/j.jallcom.2017.06.143.

[46] Z. Hua, S. Zhu, B. An, T. Iijima, C. Gu, J. Zheng, The finding of hydrogen trapping at phase boundary in austenitic stainless steel by scanning Kelvin probe force microscopy, Scr. Mater. 162 (2019) 219–222. https://doi.org/10.1016/j.scriptamat.2018.11.020.

[47] R.M. Al Qassab, Effect of Cold Work on Tensile Properties During Annealing Process for Pure Commercial Aluminum (AA 1070 Alloy), Mater. Manuf. Process. 22 (2007) 922–927. https://doi.org/10.1080/10426910701451812.

[48] O.V. Mishin, A. Godfrey, D. Juul Jensen, N. Hansen, Recovery and recrystallization in commercial purity aluminum cold rolled to an ultrahigh strain, Acta Mater. 61 (2013) 5354–5364. https://doi.org/10.1016/j.actamat.2013.05.024.

[49] A. Bałkowiec, J. Michalski, H. Matysiak, K.J. Kurzydlowski, Influence of grain boundaries misorientation angle on intergranular corrosion in 2024-T3 aluminium, Mater. Sci.-Pol. 29 (2011) 305–311. https://doi.org/10.2478/s13536-011-0050-4.

[50] L. Lacroix, L. Ressier, C. Blanc, G. Mankowski, Statistical Study of the Corrosion Behavior of Al_2CuMg Intermetallics in AA2024-T351 by SKPFM, J. Electrochem. Soc. 155 (2008) C8-C15. DOI:10.1149/1.2799089.

[51] C. Larignon, J. Alexis, E. Andrieu, L. Lacroix, G. Odemer, C. Blanc, Combined Kelvin Probe Force Microscopy and Secondary Ion Mass Spectrometry for hydrogen detection in corroded 2024 aluminium alloy, Electrochim. Acta, 110 (2013) 484-490. DOI:10.1016/j.electacta.2013.02.063.

[52] S. Evers, C. Senöz, M. Rohwerder, Spatially resolved high sensitive measurement of hydrogen permeation by scanning Kelvin probe microscopy, Electrochim. Acta, 110 (2013) 534-538. https://doi.org/10.1016/j.electacta.2013.04.171.

[53] C. Senöz, S. Evers, M. Stratmann, M. Rohwerder, Scanning Kelvin Probe as a highly sensitive tool for detecting hydrogen permeation with high local resolution, Electrochem. Comm., 13 (2011) 1542-1545. https://doi.org/10.1016/j.elecom.2011.10.014.

[54] L. Oger, M.C. Lafouresse, G. Odemer, L. Peguet, C. Blanc, Hydrogen diffusion and trapping in a low copper 7xxx aluminium alloy investigated by Scanning Kelvin Probe Force Microscopy, Mat. Sci. & Eng. A, 706 (2017) 126-135. https://doi.org/10.1016/j.msea.2017.08.119.

[55] E. Charitidou, G. Papapolymerou, G.N. Haidemenopoulos, N. Hasiotis, V. Bontozoglou, Characterization of trapped hydrogen in exfoliation corroded aluminium alloy 2024, Scr. Mater. 41 (1999) 1327–1332. https://doi.org/10.1016/S1359-6462(99)00292-4.

[56] H. Kamoutsi, G.N. Haidemenopoulos, H. Mavros, C. Karantonidis, P. Floratos, Z. Alhosani, P. Cho, D.H. Anjum, F. Ravaux, K. Polychronopoulou, Effect of precipitate coherency on the corrosion-induced hydrogen trapping in 2024 aluminum alloy, Int. J. Hydrog. Energy. 46 (2021) 34487–34497. https://doi.org/10.1016/j.ijhydene.2021.08.005.

[57] H. Kamoutsi, G.N. Haidemenopoulos, V. Bontozoglou, S. Pantelakis, Corrosion-induced hydrogen embrittlement in aluminum alloy 2024, Corros. Sci. 48 (2006) 1209–1224. https://doi.org/10.1016/j.corsci.2005.05.015.

[58] J.R. Scully, G.A. Young Jr., S.W. Smith, Hydrogen Solubility, Diffusion and Trapping in High Purity Aluminum and Selected Al-Base Alloys, Mater. Sci. Forum. 331–337 (2000) 1583–1600. https://doi.org/10.4028/www.scientific.net/MSF.331-337.1583.

[59] H. Kamoutsi, G.N. Haidemenopoulos,V. Bontozoglou, P.V. Petroyiannis, Sp.G. Pantelakis, Effect of prior deformation and heat treatment on the corrosion-induced hydrogen

trapping in aluminium alloy 2024, Corros. Sci., 80 (2014) 139–142. https://doi.org/10.1016/j.corsci.2013.11.021.

[60] A. Oudriss, F. Martin, J. Creus, J. Bouhattate, L. Marchetti, X. Feaugas, Contributions of polarized dislocation walls, internal stresses and vacancies on hydrogen trapping processes in tensile strengthening (100) nickel single crystal, Acta Mater. 245 (2023) 118622. https://doi.org/10.1016/j.actamat.2022.118622.

[61] D. Zahn, H. Tlatlik, D. Raabe, Modeling of dislocation patterns of small- and high-angle grain boundaries in aluminum, Comput. Mater. Sci. 46 (2009) 293–296. https://doi.org/10.1016/j.commatsci.2009.02.036.

[62] Mechanics – Microstructure – Corrosion coupling. Concepts, experiments, modeling and cases. Edited by Christine Blanc and Isabelle Aubert, ISTE Press and Elsevier, Publication date: 19th february 2019. ISBN 9781785483097

[63] M.- C. Lafouresse, M.-L. de Bonfils-Lahovary, L. Laffont, C. Blanc, Hydrogen mapping in aluminum alloy using an alternating current scanning electrochemical microscope (AC-SECM), Electrochem. Com. 80 (2017) 29–32. https://doi.org/10.1016/j.elecom.2017.05.007.

[64] X. Verdalet-Guardiola, R. Saillard, B. Fori, S. Duluard, C. Blanc, Comparative analysis of the anti-corrosive properties of trivalent chromium conversion coatings formed on 2024-T3 and 2024-T351 aluminium alloys, Corros. Sci. 167 (2020) 108508. https://doi.org/10.1016/j.corsci.2020.108508.

Captions of the figures

Fig. 1. Identification of the nature of the corroded GBs using EBSD analysis (inverse pole figure and band contrast figure with LAGBs, RHAGBs and CSL HAGBs) of a non-corroded sample combined with SEM/BSE image of the same area after corrosion test.

Fig. 2. SEM observation of a corroded sample and identification of the corroded areas (5 corroded areas are counted here).

Fig. 3. Band contrast map obtained by EBSD for the non-corroded 2024 Al alloy sample, where LAGBs (grey lines), RHAGBs (black lines) and CSL HAGBs (red lines) can be distinguished.

Fig. 4. a) Distribution (in cumulative length) of the GBs present in the non-corroded 2024 Al alloy as a function of their level of misorientation. The insert shows the distribution (in cumulative length) of the CSL HAGBs. b) Total fractions of LAGBs, RHAGBs and CSL HAGBs calculated by considering the cumulative length of each type of GBs.

Fig. 5. BSE-SEM images of the 2024 Al alloy after continuous immersion tests in 5 mM NaCl with various immersion times a) 8 h, b) 24 h, c) 72 h and d) 168 h, and after cyclic corrosion tests with e) 1 elementary cycle, f) 3 elementary cycles and g) 7 elementary cycles. Elementary cycle = 8 h immersion in 5 mM NaCl + 16 h emersion in air.

Fig. 6. Number of corroded GBs (a, b, c) and I_{cs} values (d, e, f) for corroded GBs of a given type after continuous immersion tests and cyclic corrosion tests. a) and d) LAGBs, b) and e) CSL HAGBs, c) and f) RHAGBs.

Fig. 7. Total length of corroded GBs after continuous immersion tests and cyclic corrosion tests, for RHAGBs, CSL HAGBs and LAGBs for continuous immersion tests (8 h, 24 h, 72 h and 168 h) and cyclic corrosion tests (1CR, 3CR and 7CR) for 2024 Al alloy.

Fig. 8. Ratio between the total length of corroded GBs and the number of corroded GBs for a given type of GB for continuous immersion tests (8 h, 24 h, 72 h and 168 h) and cyclic corrosion tests (1CR, 3CR and 7CR) for 2024 Al alloy. a) LAGBs, b) CSL HAGBs and c) RHAGBs.

Fig. 9. Number of corroded areas for the 2024 Al alloy after continuous immersion tests (8 h, 24 h, 72 h and 168 h) and cyclic corrosion tests (1CR, 3CR and 7CR).

Fig. 10. Number of corroded GBs and I_{cs} values for corroded GBs of a given type. a) and d) LAGBs, b) and e) CSL HAGBs, c) and f) RHAGBs. Results are given for 24h continuous immersions in 5 mM, 10 mM and 100 mM NaCl solutions.

Fig. 11. Total length of corroded GBs for 24h continuous immersions in 5 mM, 10 mM and 100 mM NaCl solutions for the 2024 Al alloy.

Fig. 12. Hydrogen content measured for 2024 Al alloy. Results are given for non-corroded sample, after continuous immersion tests (8, 24 h, 72 h and 168 h) and after cyclic corrosion tests (1CR, 3CR and 7CR).

Fig. 13. SKPFM analysis of corroded 2024 Al alloy a) and d) SEM images, b) and e) SKPFM maps, c) and f) Volta potential profiles obtained after 24h continuous immersion test (a, b, c) and after 1CR test (d, e, f).

Fig. 14. SKPFM analysis of corroded 2024 Al alloy. SKPFM maps plotted after a) 1CR test, b) 1 CR test followed by a 2h heat treatment at 425°C, c) 1 CR test followed by two heat treatments (2h at 425°C + 2h at 500°C), d) 1 CR test followed three heat treatments (2h at 425°C + 2h at 500°C + 2h at 530°C). SEM image of the corroded sample is shown in the insert of a). e) Volta potential profiles corresponding to SKPFM maps shown in a) –d). f) Volta potential profiles plotted after 24hCI test (SKPFM map shown in Fig. 13b) and after different heat treatments are also given for comparison: Volta potential profiles plotted immediately after 24h CI test and after an additional 2h heat treatment at 425°C are those given in Fig. 13 c).

Fig. 15. TDS analysis of corroded 2024 Al alloy a) TDS spectrum plotted after a 3CR test, b) total ratios of hydrogen trapped in P1 to P4 traps for continuous immersion tests (24 h and 72 h) and cyclic corrosion test (3CR).